# Variational Boussinesq model for strongly nonlinear dispersive waves

C. Lawrence [a],[*], D. Adytia [a],[b], E. van Groesen [a],[b]

[a] *LabMath-Indonesia, Bandung, Indonesia*
[b] *Applied Mathematics, University of Twente, Netherlands*

## HIGHLIGHTS

- A fully nonlinear Variational Boussinesq Model (FN-VBM) is derived for strong nonlinear waves.
- For strongly nonlinear waves, the dispersion quality is improved by new algorithm which minimize the kinetic energy based on deformed spectrum.
- FN-VBM is tested with various experiment (1D and 2D) and the results show a good agreement with experimental data.

## ARTICLE INFO

## ABSTRACT

For wave tank, coastal and oceanic applications, a fully nonlinear Variational Boussinesq model with optimized dispersion is derived and a simple Finite Element implementation is described. Improving a previous weakly nonlinear version, high waves over flat and varying bottom are shown to be simulated with high accuracy for a number of different cases consisting of solitary wave propagation, a focused wave above flat bottom, irregular waves over deep water, waves over a submerged bar with steep slopes (up to 1:2) and waves over shoals.

© 2017 Elsevier B.V. All rights reserved.

## 1. Introduction

The simulation of the evolution of surface gravity waves above a layer of incompressible, inviscid fluid is greatly simplified by assuming the flow to be irrotational. Such so-called potential flow simulations are often used for a large variety of applications, among which the design of waves for wave tank experiments, for coastal applications such as wave entrance in harbours and detection of long wave generation near loading or off-loading positions of oil and gas tankers, and for oceanic waves to test green water on ships. This paper deals with an improvement of previous Variational Boussinesq models in such a way that highly nonlinear waves can be simulated with sufficiently accurate dispersive properties.

In general, Boussinesq-type of equations are characterized by the fact that a dimension reduction is achieved by deriving the continuity and momentum equation at the free surface while taking the effect of the interior flow into approximate account. The free surface quantities are the surface elevation and the potential (or a velocity) at the free surface. Starting with Boussinesq [1], approximate equations were derived using series expansions to a certain order in dimensionless variables for the wave height $a/h_0$ and the inverse wave length $kh_0$ where $a$ is a characteristic amplitude, $k$ is a characteristic wave number, and $h_0$ is the water depth. The numerous classes of equations that were derived differ from each other in accuracy,

---

* Correspondence to: LabMath-Indonesia, Jl. Dago Giri no 99, Warung Caringin, Mekarwangi, 40391 Bandung, Indonesia.
  *E-mail address:* lawrence@labmath-indonesia.org (C. Lawrence).

depending on the class of waves being studied. Examples are the Boussinesq equations of Peregrine [2], Madsen et al. [3], Nwogu [4]. Discretized with several numerical methods such as finite difference, finite elements, such codes are being used widely.

Although the series expansion in the two essential parameters is intuitively attractive, a disadvantage is that using approximations of the Laplace equation with expansions in the dynamics may lead to equations that are not energy conserving and may be unstable; a required improvement may have higher order terms not sought for in the first place in the series expansion.

A different way of looking at the equations opened a new way to derive approximations in a consistent straightforward way. Zakharov [5] and Broer [6] independently observed that the surface equations can be formally described as a set of Hamilton equation with surface elevation $\eta$ and potential at the surface $\phi$ as canonical variables, a structure well-known in Classical Mechanics for finite dimensional systems. The Hamiltonian is the total energy, the sum of potential and kinetic energy. Miles [7] showed later that actually the equations can directly be obtained from an action principle which is a reformulation of the Bernoulli pressure principle that had been studied for partial results by Bateman [8] and Luke [9].

Starting with the Hamiltonian formulation, Dommermuth & Yue [10] expressed the vertical surface velocity in terms of $\eta$ and $\phi$ by Taylor expansion; West et al. [11] improved an inconsistency in the order of truncation in the continuity and momentum equation that led to instability. Both models became known as Higher Order Spectral (HOS) methods.

For the exact Hamiltonian system, without expansions or truncations for numerical purposes, the right hand side of the continuity equation is the Dirichlet-to-Neumann (DtN) operator, and it turns out that the nonlinear term in the momentum equation can be expressed explicitly in this DtN operator. In the so-called DtN approach (see Craig & Sulem [12], Bateman et al. [13]), the DtN operator is expanded in order of $\eta$. Extensions of the DtN modelling include e.g. moving bottoms by Guyenne & Nicholls [14] and 3D formulations by Xu & Guyenne [15]; see the review by Wilkening and Vasan [16] for various methods to compute the DtN operator. Schaffer [17] showed that the continuity equation in the DtN model in [12] & [13] and in HOS methods [11] & [10] are the same, but that the momentum equation in the DtN approach introduces additional terms that lead to loss of the Hamiltonian structure.

Just as the models above, we exploit the Hamiltonian formulation but follow a different way to obtain Hamiltonian consistent approximations that can be used for relatively simple discretizations. In the Hamiltonian formulation the kinetic energy is the problematic quantity; being the squared velocity integrated over the fluid domain, it is certainly positive definite, but for use in the Hamiltonian system, it has to be expressed in the canonical variables. This can only be done approximately because except for a strip domain no closed form solutions are known for the Laplace problem. Starting with Klopman et al. [18], explicit approximations of the kinetic energy were obtained by substituting explicit approximations for the internal flow in the kinetic energy expression, guaranteeing positive definiteness and stability beforehand. In Adytia & van Groesen [19], and Lakhturov et al. [20] a superposition of a few generalized Airy profiles as internal flow led to the so-called weakly nonlinear Variational Boussinesq Model (VBM) with optimized dispersion. The optimization is tailor made depending on the problem based on the spectrum of the input waves. From Dirichlet's principle, the best approximation is obtained by minimizing the kinetic energy expression with respect to the unspecified parameters which are the wave numbers of the chosen Airy profiles. Then dispersion can be made accurate until $kh_0 \approx 20$ with only 3 Airy functions. Numerical discretizations of the canonical variables, in this paper using Finite Elements, then leads to a consistent finite dimensional Hamiltonian system that has inherited the positive definiteness properties and resulting stability in the dynamics. For time marching, sufficiently accurate explicit time advancing methods are used. It turned out that for waves with moderate wave heights, the code performed as expected in a large range of wave types and various bathymetries.

In this paper we will improve on these last results by taking the nonlinearity in full account (which was not done in the weakly nonlinear variant), and by improving the optimization procedure. This will result in a numerical code that is able to deal with highly nonlinear waves while retaining good dispersive properties. The organization of the rest of the paper is as follows.

In Section 2 (with some detailed formulas in Appendix) the fully nonlinear Variational Boussinesq Model (abbreviated as FN-VBM) is derived, and the improvement of the optimization procedure in Lakhturov et al. [20] is described. In Section 3 the numerical implementation with a Finite Element method is outlined. In Section 4 simulations for various by now classical experiments are compared with measured data, showing the improved performance of the presented model; the cases deal with a focused wave above flat bottom, irregular waves over deep water, waves over a submerged barge with steep slopes (up to 1:2) and waves over shoals.

## 2. Variational Boussinesq model

The basic principles on which Variational Boussinesq models are based are the Hamiltonian description of the surface waves above irrotational flow. In previous papers we used Dirichlet's minimization principle to approximate the kinetic energy functional in canonical variables in a consistent way; in this paper we will improve the approximation such that highly nonlinear waves can be simulated accurately using optimized dispersive properties.

In the first subsection we will resume the Hamiltonian formulation and introduce the kinetic energy in its dependence on the canonical variables. Although uniquely defined, this kinetic energy cannot be obtained in an explicit form, since it requires the solution of the Laplace problem in the fluid domain. Therefore we will use Dirichlet's principle in the second subsection to obtain approximations of the kinetic energy to arrive at consistent Hamiltonian approximations of the surface wave problem,

with the Fully Nonlinear VBM formulation as result. In the last subsection, exploiting once again the minimizing property of Dirichlet's principle, free parameters in the approximation can be optimized using information from influx or initial data of the wave problem, which will produce 'tailor made' optimal dispersive properties.

In the following we will use $\mathbf{x} = (x, y)$ to denote the horizontal coordinates, $z$ for the vertical direction, and $z = h(\mathbf{x})$ describes the bathymetry. The constant density of the incompressible, inviscid fluid is taken to be $\rho = 1$ and will be suppressed in the following. The gravitational constant will be denoted as usual by $g$.

### 2.1. Hamiltonian formulation of surface waves

The Hamiltonian formulation was obtained by Zakharov [5] for waves on infinite depth and by Broer [6] for waves above a flat bottom. Using as canonical variables the surface elevation $\eta(x, t)$ and the potential at the free surface $z = \eta(x, t)$, the equations are given by the Hamilton equations

$$\begin{cases} \partial_t \eta = \delta_\phi \mathcal{H}(\phi, \eta) \\ \partial_t \phi = -\delta_\eta \mathcal{H}(\phi, \eta) \end{cases} \tag{1}$$

where $\delta_\phi \mathcal{H}$ and $\delta_\eta \mathcal{H}$ denote the variational derivatives of the Hamiltonian $\mathcal{H}(\phi, \eta)$ with respect to $\phi$ and $\eta$ respectively. The Hamiltonian is numerically the total energy, which is the sum of the kinetic and the potential energy. The potential energy $P$ only depends on $\eta$ and is given by

$$P(\eta) = \frac{1}{2} \int_{\mathbf{x}} g\eta^2 \, d\mathbf{x}.$$

The kinetic energy is given by the Dirichlet integral

$$D(\Phi) = \frac{1}{2} \int_{\mathbf{x}} \int_{-h}^{\eta} |\nabla_3 \Phi|^2 dz d\mathbf{x}$$

where $\Phi$ has to satisfy the Laplace equation in the interior: $\Delta \Phi = 0$, the prescribed surface condition $\Phi = \phi$ at $z = \eta$, the impermeability of the, possibly varying, bottom $\partial_n \Phi = 0$ at $z = -h(x)$ and suitable boundary conditions that guarantee that the flow vanishes at lateral boundaries far away from the region in which the waves are studied. Dirichlet's principle states that this flow can be found as the unique minimizer of

$$K(\phi, \eta) = Min \{D(\Phi) | \Phi = \phi \text{ at } z = \eta\}. \tag{2}$$

This then defines the kinetic energy as functional of the two canonical variables and the Hamiltonian is given by

$$\mathcal{H}(\phi, \eta) = K(\phi, \eta) + P(\eta).$$

It turned out that the Hamiltonian formulation can be directly obtained from the pressure principle of Bateman [8] and Luke [9], written as the action principle with the Bernoulli pressure as Lagrangian density

$$\mathcal{L} = -\int \left[ \int_{\mathbf{x}} \int_{-h}^{\eta} \left\{ \partial_t \Phi + \frac{1}{2} |\nabla_3 \Phi|^2 + gz \right\} dz d\mathbf{x} \right] dt. \tag{3}$$

By taking the time derivative in $\partial_t \Phi$ out of the integration domain and omitting an inessential total time derivative, Miles [7] showed that a canonical action principle results in the form

$$\mathcal{L} = \int \left[ \int \phi \partial_t \eta d\mathbf{x} - \mathcal{H}(\eta, \phi) \right] dt \tag{4}$$

from which variations with respect to $\eta$ and $\phi$ directly produce the Hamiltonian equations.

The Hamilton equations can be specified as

$$\begin{cases} \partial_t \eta = \delta_\phi K \equiv \partial_N \Phi|_{z=\eta} \\ \partial_t \phi = -g\eta - \delta_\eta K(\phi, \eta) \end{cases} \tag{5}$$

where $\partial_N \Phi|_{z=\eta} = \nabla_3 \Phi \cdot N = \partial_z \Phi - \nabla \eta \cdot \nabla \Phi|_{z=\eta}$ is the directional derivative in the normal direction $N = (-\nabla \eta, 1)$ at the free surface, the so-called Dirichlet-to-Neumann operator. Note that actually $\partial_N \Phi = \sqrt{1 + (\partial_x \eta)^2} \partial_n \Phi$ with $n = N/\sqrt{1 + (\partial_x \eta)^2}$ the normal at the free surface;

### 2.2. Consistent approximations of the kinetic energy

In order to arrive at a practically useful model, the kinetic energy functional has to be expressed in the canonical variables in an explicit way. Since the Laplace problem can only be solved with Airy's theory for a strip, an explicit expression can only be obtained in an approximate way. Starting with Broer et al. [21,22], such approximations were constructed in a consistent way by Klopman et al. [18], Adytia & Van Groesen [19], and others. The consistency refers to the fact that approximations of the kinetic energy again leads to a Hamiltonian system for which the total energy is a constant of the motion. Furthermore, if

approximations for the potential are taken in the Dirichlet integral as we will do in this paper, the kinetic energy density will remain positive definite. Together with the fact that the related approximate Hamiltonian will be conserved exactly during the evolution, this implies some form of stability.

The simplest approximation is to take $\Phi(x, z) = \phi(x)$ in the total fluid domain. Then the kinetic energy is easily found to be $K_{SW}(\phi, \eta)$

$$K_{SW}(\phi, \eta) = \int (h + \eta) |\nabla\phi|^2 dx \tag{6}$$

which leads to the shallow water equations, to be expected from the Ansatz for $\Phi$.

More sophisticated methods use the extension of this idea by adding $z$-dependence as in Klopman et al. [18]

$$\Phi(\mathbf{x}, z, t) = \phi(\mathbf{x}, t) + \Sigma_m F_m(z, \eta, h) \psi_m(\mathbf{x}, t) = \phi + F \cdot \Psi \tag{7}$$

where $F$ and $\psi$ are vector functions. To keep the canonical structure of the Hamiltonian, it is required that $\Phi(\mathbf{x}, z, t) = \phi(\mathbf{x}, t)$ at $z = \eta$, i.e. that $F_m(z = \eta) = 0$ for any $m$. The vertical profiles $F_m$ will be chosen in advance, but the spatial amplitude functions $\psi_m(\mathbf{x}, t)$ will be determined in the dynamic evolution. Substituting the approximation of $\Phi$ in (7) into the Dirichlet integral results in

$$K_{VBM} = \frac{1}{2} \int_{\mathbf{x}} \int_{-h}^{\eta} |\nabla\phi + \nabla(F \cdot \Psi)|^2 + (\partial_z F \cdot \Psi)^2 \, dz d\mathbf{x}$$
$$= \frac{1}{2} \int_{\mathbf{x}} \int_{-h}^{\eta} |\nabla\phi + F \cdot \nabla\Psi + \nabla F \cdot \Psi|^2 + (\partial_z F \cdot \Psi)^2 \, dz d\mathbf{x}. \tag{8}$$

Slightly different from the normalization as in Klopman [23], following Adytia & Van Groesen [19], we choose the functions $F$ as hyperbolic-cosine functions from Airy's theory, adjusted to satisfy $F_m(z = \eta) = 0$

$$F_m(z; \eta, h) = \frac{\cosh(\kappa_m(z + h))}{\cosh(\kappa_m(\eta + h))} - 1. \tag{9}$$

Here the wavenumbers $\kappa_m$ are constants, that will be optimally chosen in the last subsection. Note that $\partial_z F = 0$ at the bottom, which will be correct only for horizontal bottom; we will remark later about the consequence of this inconsistency when dealing with varying bottoms. The case of deep water will be obtained in the limit $h \to \infty$.

Substituting the approximation of $\Phi$ in (7) into the kinetic energy functional results in

$$K_{VBM}(\phi, \eta; \Psi, \kappa) = \frac{1}{2} \int_{\mathbf{x}} \int_{-h}^{\eta} |\nabla\phi + \nabla(F \cdot \Psi)|^2 + (\partial_z F \cdot \Psi)^2 \, dz d\mathbf{x}$$
$$= \frac{1}{2} \int_{\mathbf{x}} \int_{-h}^{\eta} |\nabla\phi + F \cdot \nabla\Psi + \nabla F \cdot \Psi|^2 + (\partial_z F \cdot \Psi)^2 \, dz d\mathbf{x}. \tag{10}$$

Taking the $z$-integrations over the expressions with $F$, the kinetic energy can be written as

$$K_{VBM}(\phi, \eta; \Psi, \kappa) = \frac{1}{2} \int_{\mathbf{x}} [(h + \eta)|\nabla\phi|^2 + \alpha\nabla\Psi \cdot \nabla\Psi + (\theta|\nabla\eta|^2 + \gamma)\Psi \cdot \Psi$$
$$+ 2\nu\nabla\eta\Psi \cdot \nabla\Psi + 2\nabla\phi(\beta \cdot \nabla\Psi + \xi\nabla\eta \cdot \Psi)]d\mathbf{x} \tag{11}$$

where matrices $\alpha$, $\gamma$, $\nu$, and $\theta$, and vectors $\beta$ and $\xi$ are introduced as

$$\alpha_{ij} = \int_{-h}^{\eta} F_i F_j dz; \quad \beta_i = \int_{-h}^{\eta} F_i dz; \quad \gamma_{ij} = \int_{-h}^{\eta} \partial_z F_i \partial_z F_j dz$$
$$\nu_{ij} = \int_{-h}^{\eta} F_i \partial_\eta F_j dz; \quad \xi_i = \int_{-h}^{\eta} \partial_\eta F_i dz; \quad \theta_{ij} = \int_{-h}^{\eta} \partial_\eta F_i \partial_\eta F_j dz. \tag{12}$$

Explicit expressions for these coefficients are given in Appendix.

Neglecting the effects of variations of $F_m$ with $x$, i.e. taking $\nabla F_m = (\partial_\eta F_m \nabla\eta + \partial_h F_m \nabla h) = 0$, leads to the so-called *weakly nonlinear* VBM from [19]. As an improvement, we will take in this paper the effects of $\partial_\eta F_m \nabla\eta$ into account, aiming at a *fully nonlinear* (FN) Variational Boussinesq model. However, contributions from bed slopes $\partial_h F_m \nabla h$ will still be neglected in the formulas below and in the numerical implementation, which means that bottom variations are dealt with in a quasi-homogeneous way. The applications in the numerical test cases will show that even for very steep slopes 1:2 this approximation is still acceptable, see for instance the Ohyama and Zou experimental test cases in Section 4.

### 2.3. VBM dynamic equations and dispersion relation

Having obtained the expression for the kinetic energy, the dynamic Hamilton equations for the fully nonlinear VBM are obtained by taking variations of $\mathcal{H}_{VBM}$ with respect to $\eta$ and $\phi$. The amplitude functions $\Psi$ are taken in accordance with

Dirichlet's minimization principle, which means that we minimize $K_{VBM}$ with respect to $\Psi$, leading to a set of compatibility equations in the form of a system of linear strongly elliptic equations. Written together, the equations become

$$
\begin{aligned}
\partial_t \eta &= -\nabla \cdot [(h + \eta) \nabla \phi + \beta \cdot \nabla \Psi + \xi \nabla \eta \cdot \Psi] \\
\partial_t \phi &= -g\eta - \frac{1}{2}|\nabla \phi|^2 - \mathcal{R} \\
\mathcal{E}(\Psi) &= \nabla \cdot (\beta \nabla \phi) - \xi \nabla \eta \nabla \phi
\end{aligned}
\tag{13}
$$

where $\mathcal{E}(\Psi)$ is the elliptic operator

$$
\mathcal{E}(\Psi) = -\nabla \cdot (\alpha \nabla \Psi) + \left(\theta |\nabla \eta|^2 + \gamma\right) \Psi + v^T \nabla \eta \nabla \Psi - \nabla \cdot (v \nabla \eta \Psi)
\tag{14}
$$

and the expression $\mathcal{R}$ is given by

$$
\begin{aligned}
\mathcal{R} &= \frac{1}{2}\partial_\eta \alpha \nabla \Psi \cdot \nabla \Psi + \frac{1}{2}\left(\partial_\eta \theta |\nabla \eta|^2 + \partial_\eta \gamma\right) \Psi \cdot \Psi \\
&+ \partial_\eta v \nabla \eta \Psi \cdot \nabla \Psi + \nabla \phi \left(\partial_\eta \beta \cdot \nabla \Psi + \partial_\eta \xi \nabla \eta \cdot \Psi\right) \\
&- \nabla \cdot (\xi \nabla \phi \cdot \Psi + v\Psi \cdot \nabla \Psi + \theta \nabla \eta \Psi \cdot \Psi).
\end{aligned}
\tag{15}
$$

Note that $\mathcal{R}$ appears as a consequence of the formulation of the Bernoulli pressure at the surface in the canonical variable $\phi$.

If we restrict to the case of a horizontal bottom at depth $h_0$ (the case of infinitely deep water is obtained in the limit $kh_0 \to \infty$), the exact dispersion relation of linear surface water waves can be written as

$$
\Omega_{ex}(k) = c_0 k \sqrt{\frac{\tanh(kh_0)}{kh_0}} \text{ with } k = |\mathbf{k}|
\tag{16}
$$

where $c_0 = \sqrt{gh_0}$ is the phase velocity for infinitely long waves. The kinetic energy for linear waves can then be written exactly as

$$
K_{lin}(\phi) = \frac{1}{4\pi g} \int \Omega_{ex}^2(k) \left|\hat{\phi}\right|^2 d\mathbf{k}
$$

with $\hat{\phi}(\mathbf{k})$ the Fourier transform of $\phi(x)$.

The kinetic energy is quadratic in the potential, so that linearized equations are obtained by taking $\eta = 0$ in $K_{VBM}$, leading to $K_{VBMlin}$. The linearized equations for VBM can then be readily obtained, and denoting all coefficients with a 0-subscript for $\eta = 0$, the dispersion relation for VBM can be found and is given by

$$
\Omega_{vbm}(k) = c_0 k \sqrt{1 - \frac{k^2}{h_0}\beta_0 \cdot \left(\alpha_0 k^2 + \gamma_0\right)^{-1}\beta_0}.
\tag{17}
$$

Here we assume that for multiple profiles all values of $\kappa_m$ in the Airy profiles (9) are different so that the matrix $(\alpha_0 \kappa^2 + \gamma_0)$ is invertible. Then, using Cauchy's inequality, it can be shown that the expression under the square root is positive definite, and so $\Omega_{vbm}(k)$ is real for each $k$ as required for stability. Observe that for given $\kappa$, the expressions for the phase and group velocity do not tend to zero in the limit $k \to \infty$; for instance for the phase velocity it holds that

$$
C_{VBM}(k) \to c_0 \sqrt{1 - \frac{1}{h_0}\beta_0 \cdot \alpha_0^{-1}\beta_0} \text{ for } k \to \infty.
$$

As an example we take the case of a Focusing Wave Group, described in Section 4.2.1. For the initial spectrum, we optimize the parameter $\kappa$ in a 3-profile approximation and show the corresponding dispersion relation, phase and group velocity in Fig. 1. Optimization of the parameters $\kappa$ will be discussed in the following section.

## 2.4. Dispersion optimization

The dispersion quality of VBM is highly determined by the choice of the parameters $\kappa_m$ in (9). This flexibility can be used to choose the number of vertical profiles and the parameters $\kappa_m$ depending on the case under investigation, as will now be shown.

The values of the parameters $\kappa$ appear in the coefficients $\alpha_0$, $\beta_0$, etc. as shown in the section above. We discuss an optimization criterion to choose optimal values for the parameters $\kappa_m$ based on an improvement of the idea in Lakhturov et al. [20]. The optimal values can be obtained from information about the initialization of the wave. Since in this paper we only use the influx of the surface elevation at a fixed position or line, we will restrict the description to this case. For notational simplicity, we will consider only one horizontal direction.
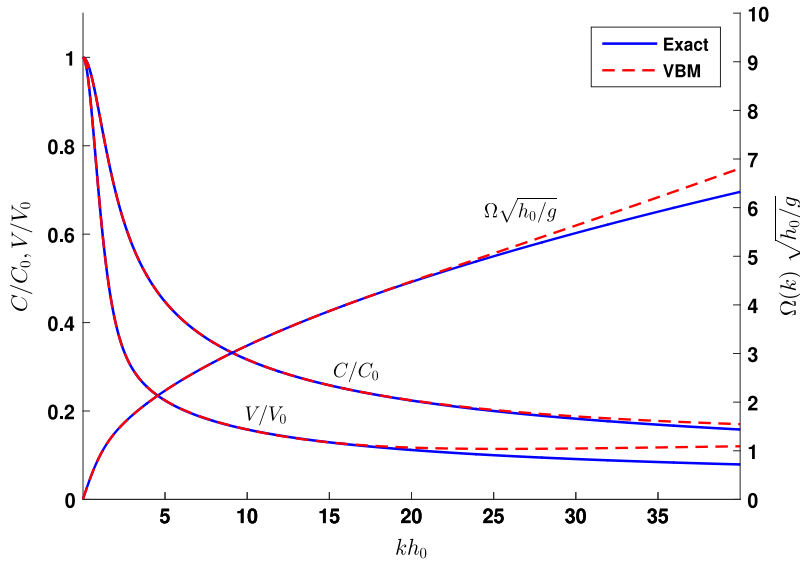
**Fig. 1.** Comparison of dispersion relation (right axis), normalized phase and group velocity (left axis) between 3 profile VBM (red dash line) and Airy linear theory (blue solid) of the Focusing Wave Group as functions of $kh_0$. (For interpretation of the references to colour in this figure legend, the reader is referred to the web version of this article.)

The kinetic energy from Dirichlet's principle (2) when restricted to $\eta = 0$ above flat bottom

$$K_{lin}(\phi) = Min \{D(\Phi) | \Phi = \phi \text{ at } z = 0\}$$

can be found explicitly with Airy theory and leads to the quadratic expression in $\phi$ using its spatial Fourier transform

$$K_{lin}(\phi) = \frac{1}{4\pi g} \int \Omega_{ex}^2(k) \left|\hat{\phi}(k)\right|^2 dk.$$

The minimizing Dirichlet property implies that for VBM-dispersion $\Omega_{VBM}(k; \kappa)$, now writing the explicit dependence on $\kappa$, it holds that

$$K_{lin}(\phi) \leq K_{VBMlin}(\phi; \kappa) = \frac{1}{4\pi g} \int \Omega_{VBM}^2(k; \kappa) \left|\hat{\phi}(k)\right|^2 dk$$

for each $\phi$ and for each choice of $\kappa$. Hence, an optimal choice would be, for given $\phi$, to choose $\kappa$ to be the minimizer of

$$\min_{\kappa} \int \Omega_{VBM}^2(k; \kappa) \left|\hat{\phi}(k)\right|^2 dk. \tag{18}$$

Of course, in a dynamic simulation, with $\phi(x, t)$ changing with time, this seems difficult to achieve. However, it turns out that for linear evolution, this is possible, while for strongly nonlinear evolutions an adaptation will be proposed below.

To optimize the parameters in $\Omega_{VBM}$ such that the dispersion is as good as possible is straightforward for an initial value problem for which $\phi = \phi_0$ would be prescribed at an initial time: then (18) can be used directly with $\phi_0$. But to deal with the influx problem, we have to express the kinetic energy in terms of the given influx signal, say at $x = 0$ the signal $s(t) = \eta(x = 0, t)$. For linear, uni-directional flow this will be achieved as follows.

The linear momentum equation $\partial_t \phi = -g\eta$ translates in spectral space into $i\Omega_{ex}(k) \hat{\phi}(k, t) = g\hat{\eta}(k, t)$. Writing $\check{s}(\omega)$ for the temporal Fourier transform of the signal $s(t)$, the evolving uni-directional wave is given by

$$\eta(x, t) = \int \check{s}(\omega) e^{iK(\omega)x - \omega t} d\omega = \int \check{s}(\Omega_{ex}(k)) e^{i(kx - \Omega_{ex}(k)t)} V(k) dk$$

where $V(k)$ is the group velocity of the exact dispersion relation that appears in the transformation from frequency to wave number. Hence $\hat{\eta}(k, t) = \check{s}(\Omega_{ex}(k)) e^{-i\Omega_{ex}(k)t} V(k)$ so that

$$\left|\hat{\phi}(k, t)\right|^2 = \left(\frac{g\check{s}(\Omega_{ex}(k)) V(k)}{\Omega_{ex}(k)}\right)^2.$$

Then

$$\int \Omega_{VBM}^2(k; \kappa) \left|\hat{\phi}(k, t)\right|^2 dk = g^2 \int \left(\frac{\Omega_{VBM}(k; \kappa)}{\Omega_{ex}(k)}\right)^2 \left|\check{s}(\Omega_{ex}(k))\right|^2 V(k)^2 dk$$
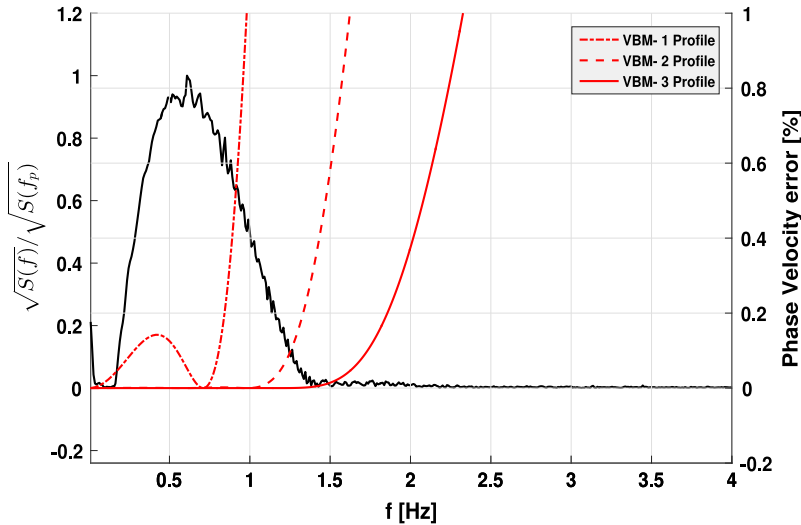
**Fig. 2.** The normalized amplitude spectrum (black solid line, left axis) of the Focusing Wave Group at $x = 10$ m is plotted together with the phase velocity error for 1, 2 and 3 profiles (red line). For 1 profile (red, dash–dot), the parameter is $f_1 = 0.71$ Hz (corresponds to $\kappa_1 = 2.09$). For 2 profiles (red, dash), the parameters are $f_1 = 0.58$ Hz and $f_2 = 0.98$ Hz (correspond to $\kappa_1 = 1.5$, $\kappa_2 = 3.87$). For 3 profiles (red, solid), the parameters are $f_1 = 0.55$ Hz, $f_2 = 0.87$ Hz and $f_3 = 1.19$ Hz (corresponds to $\kappa_1 = 1.38$, $\kappa_2 = 3.06$, $\kappa_3 = 5.7$). (For interpretation of the references to colour in this figure legend, the reader is referred to the web version of this article.)

which can be rewritten, using the notation $K(\omega)$ to denote the inverse of the exact dispersion relation, as

$$\int \Omega_{VBM}^2(k; \kappa) \left| \hat{\phi}(k, t) \right|^2 dk = g^2 \int \left| \check{s}(\omega) \right|^2 \left( \frac{\Omega_{VBM}(K(\omega); \kappa)}{\omega} \right)^2 V(K(\omega)) \, d\omega. \tag{19}$$

In this last expression only the *spectrum* $S(\omega) = \left| \check{s}(\omega) \right|^2$ of the initial signal appears in the right hand side. Hence, for linear evolution the parameters $\kappa$ that appear in $\Omega_{VBM}$ can be optimized for the given spectrum according to the Dirichlet principle, which parameters are then optimal for all successive time.

Concerning the above, a few remarks are in order. First about a limitation of the method. For linear evolution above flat bottom it is well known that the spectrum $\left| \check{s}(\omega) \right|^2$ is independent of time, what is shown and used above. But the initial spectrum will deform during the evolution when (strong) nonlinear effects and/or large bottom variations are present. As a consequence, at positions downstream the influx position the parameters $\kappa$ will not be optimal anymore. If a strongly deformed spectrum can be expected, for instance a very much broadening of the spectrum, it may be better to use (an approximation) of the deformed spectrum to optimize the parameters; a trial simulation may indicate such deformations and provide an approximation of the deformed spectrum. An example is given for the strong focusing wave in Section 4.2.1. Fig. 2 shows the error of the phase velocity for 1, 2 and 3 profiles with optimized parameters $\kappa$ using the spectrum of the initial elevation signal. Very close to the focusing point, short waves are generated, and the spectrum widens considerably, as seen in Fig. 3. The optimal values of $\kappa$ (translated to optimal frequencies in Hz) for the initial and widened spectrum changes for 3 profiles from (0.55, 0.87, 1.19) to (0.60, 1.03, 1, 94) respectively, a difference that is well noticeable in results of the simulation.

Another remark is about the difference with the expression in Lakhturov et al. [20]. In that paper, in the proposed functional to be minimized, the value of the potential $\phi_0$ used in the optimization was obtained from the initial signal $s_0(t)$ using the VBM dispersion. In doing so, this function differs from the evolution with the exact dispersion, so that the minimization argument is only approximate compared to the correct formulation above. Especially for very broad spectra the method above will be more accurate, in particular for the larger optimized parameters in a two or three profile optimization.

## 3. Numerical implementation

The approach towards the surface wave problem as formulated in the previous section is also followed for the numerical implementation. That is, we will keep the dynamical Hamiltonian structure in the process to go from the space continuous formulation to the finite dimensional spatial discretization, described in the first subsection. This will lead to a fully consistent finite dimensional Hamiltonian system with exact conservation of the positive definite energy and stability as consequence. The dynamic system will then be evolved in time using a standard, accurate time discretization method, avoiding implicit schemes, in the second subsection. Some other aspects of the numerical scheme will be discussed in the last subsection.
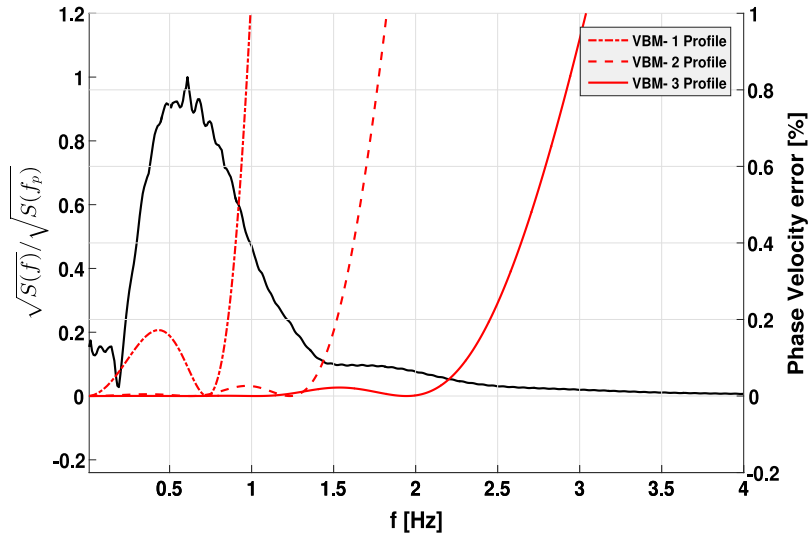
**Fig. 3.** The normalized amplitude spectrum (black solid line, left axis) of the Focusing Wave Group at $x = 50$ m is plotted together with the phase velocity error for 1, 2 and 3 profile (red line). For 1 profile (red, dash–dot), the parameter is $f_1 = 0.73$ Hz (corresponds to $\kappa_1 = 2.2$). For 2 profiles (red, dash), the parameters are $f_1 = 0.63$ Hz and $f_2 = 1.23$ Hz (corresponds to $\kappa_1 = 1.71, \kappa_2 = 6.09$). For 3 profiles (red, solid), the parameters are $f_1 = 0.60$ Hz, $f_2 = 1.03$ Hz and $f_3 = 1.94$ Hz (corresponds to $\kappa_1 = 1.58, \kappa_2 = 4.27, \kappa_3 = 15.1$). (For interpretation of the references to colour in this figure legend, the reader is referred to the web version of this article.)

### 3.1. Spatial discretization

The kinetic energy functional of VBM (11) contains at most quadratic first order derivatives of the basic quantities. Therefore a Finite Element implementation is chosen with piecewise linear (pwl) splines to reduce the computational complexity. The canonical variables, the amplitude functions and the depth are therefore approximated with a finite sum of spline functions. Illustrated for the surface elevation,

$$\eta(x, t) \approx \Sigma_{m=1}^{N} \bar{\eta}_m(t) T_m(x) \tag{20}$$

with $T_m(x)$ a pwl spline on a predefined regular or irregular grid. In our implementation we use an irregular grid with adaptive mesh width depending on the depth variations, especially useful for coastal zone simulations [24]. Writing a bar over the temporal vector functions multiplying the splines as in (20), insertion in the continuous kinetic energy and Hamiltonian leads to the discretized versions $\bar{K}_{VBM}(\bar{\phi}, \bar{\eta}; \bar{\psi}, \kappa)$ and $\bar{\mathcal{H}}(\bar{\phi}, \bar{\eta})$ and the finite dimensional system of equations

$$\begin{cases} M\partial_t \bar{\eta} = \delta_{\bar{\phi}} \bar{\mathcal{H}}_{VBM}(\bar{\phi}, \bar{\eta}) \\ M\partial_t \bar{\phi} = -\delta_{\bar{\eta}} \bar{\mathcal{H}}_{VBM}(\bar{\phi}, \bar{\eta}) \\ \delta_{\bar{\psi}} \bar{K}_{VBM}(\bar{\phi}, \bar{\eta}; \bar{\psi}, \kappa) = 0. \end{cases} \tag{21}$$

Here $M$ is a positive definite mass matrix, custom in FE methods.

The optimal wave numbers $\kappa$ are obtained as described above as the minimizers of the finite dimensional function $\bar{K}_{VBM}(\bar{\phi}, \bar{\eta}; \bar{\psi}, \kappa)$.

For 1D, the finite dimensional variant of the elliptic equation for the amplitude vectors $\bar{\psi}$ is solved using direct method such as the Thomas Algorithm since our matrix in the linear system of equations is tridiagonal (1 profile) or block tridiagonal (multiple profiles). For 2D, the matrix system can be very large due to multiple profiles and a large number of elements. Since we use a Finite Element implementation with piecewise linear splines, the matrix system is very sparse and are solved using iterative methods such as pre-conditioned biconjugate gradient stabilized method (MATLAB function 'bicgstab', see [25]) with initial guess that is obtained from the previous time steps.

### 3.2. Initialization and time stepping

For the influx problems we will consider in this paper, the prescribed elevation signal at a point or line in the interior domain is dealt with by adding a source term to the dynamic equations as described in Lie et al. [26]. No second or higher order steering has been applied. To prevent unwanted oscillations, a spatial adaptation zone has been used as described in that reference.

In the time stepping process, to advance one timestep, we use the updated values of $\bar{\phi}, \bar{\eta}$ to determine the corresponding $\bar{\psi}$ by solving the discretized elliptic equation. After that the right hand sides of the dynamic equations can be determined and the time step can be made.

For the cases described in the next section, the standard time evolution ode23-code from matlab was used.

It has been observed, for two cases described in the next section, namely Ohyama et al. experiment and the deep water case, that the fully nonlinear VBM may develop very high wave numbers due to the spatial nonlinear interactions, leading to short period wiggles in the time signal. This has been prevented by filtering the output after each 50 or 100 time steps. The grid spacing $\Delta x$ should be able to represent the shortest wave component (e.g. one wave can be well represented by 12 grid points). This grid spacing $\Delta x$ leads to a largest wave number $k$, which corresponds to largest possible frequency by Airy dispersion and will be the cut-off frequency ($f_{cut}$) for the filtering. Another method would be to filter the right handsides in space.

### 3.3. Other numerical aspects

Damping zones with a Sommerfeld transparent boundary at the end of the zone for long waves were used to diminish the waves approaching the boundary of the numerical domain and to prevent reflection back into the numerical domain, as in Adytia & Van Groesen [19].

## 4. Simulation results compared to experimental data

In four subsections we show results of simulations compared with experimental data; to show the improvements using the fully nonlinear code, we also compare for some cases with simulations using the weakly nonlinear code. In the first subsection we deal with solitary wave propagation over flat bottom. In the second subsection we deal with broad-band spectrum waves, namely a strong focusing wave above flat bottom and a wave with JONSWAP spectrum in deep water. In the next subsection, we show results for 3 cases of harmonic waves over submerged bars with various lay-out, and in the last subsection we consider shoaling properties for two different lay-outs. In addition, in Adytia & Lawrence [27] results can be found of simulations for regular and irregular waves propagating above a submerged bar (Beji–Battjes [28]) and the dam-break problem of Wei et al. [29] of an undular bore propagating into still water above constant depth.

### 4.1. Solitary wave propagation over flat bottom

The first test case is solitary wave propagation over constant depth. In Classical Mechanics with Hamiltonian dynamics, relative equilibria are non-steady motions that are steady in some moving frame of reference; the standard example is a rotating mass point at the end of an inextensible wire that rotates with constant height of the mass depending on the value of the angular momentum. In a similar way, in one-directional Hamiltonian wave dynamics there is, except the Hamiltonian, for waves about flat bottom another invariant integral, namely the horizontal momentum, $M = \int u\eta dx$ that corresponds to a dynamics that is uniform translation. Critical points of the total energy $H$ on level sets of $M$ then correspond to steadily translating specific wave forms satisfying $\delta H = \lambda M$ (variations with respect to both canonical variables), where $\lambda$ is the translation velocity. Confined wave forms are commonly called, after the work of Korteweg–de Vries 1894, solitary waves (travelling faster than the largest phase speed of linear waves), while their periodic equivalents are the cnoidal waves, with lower speed.

For the present VBM equations, the approximated and discretized Hamiltonian and horizontal momentum functions are conserved, and hence simulations should, up to numerical time integration errors, support such steady waves. To test this for solitary waves, we took the solitary wave data of the exact Euler equations calculated by Dutykh and Clamond [30] as input for the VBM simulations. We show results for the rather extreme case of height 0.6 above depth $D = 1$; see Fig. 4 for the initial conditions for the free surface $\eta$ and the velocity potential $\phi$.

In Fig. 5 , we show the results for the fully nonlinear FN-VBM simulation; this simulation retains both shape and speed of the Euler solitons, even for this extreme case. In Fig. 7, it is shown that the maximum $L_1$ error ('energy') $E(t) = \int |\eta(x, t)|^2 dx$ relative to the initial value is less than 0.014%.

As can be expected, the weakly nonlinear VBM is not capable to retain the initial shape as shown in Fig. 6. But interestingly enough, after shedding off some (slower) waves, for increasing time the shape deforms to a state that tends to a solitary wave again, but now with shape and speed that corresponds to the (less accurate) Hamiltonian of the weakly nonlinear WN-VBM. This shows that even poorer Hamiltonian approximations do carry the essential dynamic wave features.

### 4.2. Broad-band spectrum waves

#### 4.2.1. Focusing wave group

A focused wave was generated at the Maritime Research Institute Netherlands (MARIN) in a wave tank with 200 m length and 1 m water depth. The influx signal is designed to generate first short period small amplitude waves, followed by higher and longer period waves. By choosing the initial phases correctly, the long waves will catch up with the short waves and the waves collide at a focusing point to form a high wave. The wave, generated by the flap motion at $x = 0$, was measured at
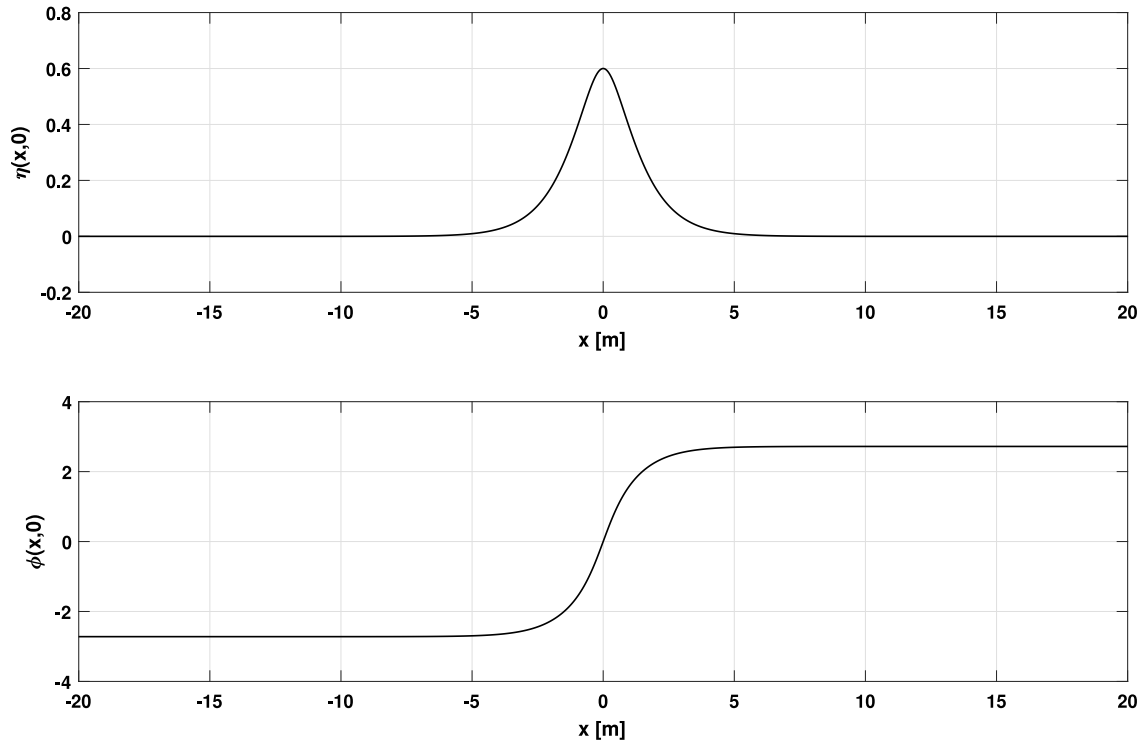
**Fig. 4.** The initial wave elevation (upper plot) and velocity potential (lower plot) of the solitary wave with height of 0.6 m.

$x_0 = 10$ m and $x_1 = 50$ m. For our simulations, the measured elevation at $x_0 = 10$ m is used as influx signal. The signal and the broad amplitude spectrum at $x_0$ are shown in Fig. 8. The dispersion plays an important role in this experiment, therefore using only one Airy profile function is not accurate enough [31]. Also nonlinearity is quite important because some white capping was observed just downstream of the focusing point.

The measurement of the elevation at $x_1$ is the only available data around the focusing position. The result of VBM is shown in Fig. 9 for both WN-VBM as well as for FN-VBM. It seems that for both codes the wave travels somewhat too fast since when we observe the time signal 0.2 m further, a better match with the measured profile is obtained as shown in Fig. 9. In Fig. 10, the wave profile at $t = 94.2$ s together with the maximum temporal amplitudes for both WN-VBM and FN-VBM is plotted. The results show that simulations with FN-VBM can produce higher and steeper waves compared to WN-VBM.

### 4.2.2. JONSWAP-type waves over deep water

An irregular wave with a spectrum of JONSWAP-type was generated at MARIN wave tank. All the parameters to be given below correspond to a spatial scaling with a factor 50.

In the experiment, the still water depth is 510 m and the waves have significant wave height approximately 9.8 m and peak period 13.9 s which correspond to $kh_0 = 10.6$ (see Fig. 11). There are five wave gauges where the wave elevation is measured: W1 at $x = 0$, W2 at $x = 275.4$ m, W3 at $x = 312.4$ m, W4 at $x = 642.6$ m and W5 at $x = 1593.4$ m. For our simulations, the measured elevation W1 is used as influx signal and grid spacing $\Delta x$ is 1.5 m which leads to $f_{cut} = 0.295$ Hz. It is clear that the dispersion is important to get the correct velocity in deep water and that the possible appearance of high, freak-type waves, requires correct nonlinear interactions.

In the simulation, the correlation has been calculated in the time interval (0;1000) s at W2, W3, W4, W5 to be 0.96, 0.96, 0.95, 0.95. As shown in Figs. 12 and 13, the very high and steep waves are well recovered by FN-VBM in deep water. In Table 1 we show the essential improvement of the Fully Nonlinear VBM results compared to the simulations with the Weakly Nonlinear VBM code; propagation speeds of the high waves are much better modelled by the FN model, indicated by the fact that the correlation between simulated and measured elevations at the measurement points remains nearly constant along the whole wave tank, while the quality of the WN results decay very fast with increasing distance, despite the fact that both methods recover approximately the same amount of wave energy along the tank, measured by the quotient of the simulated and measured potential energy.
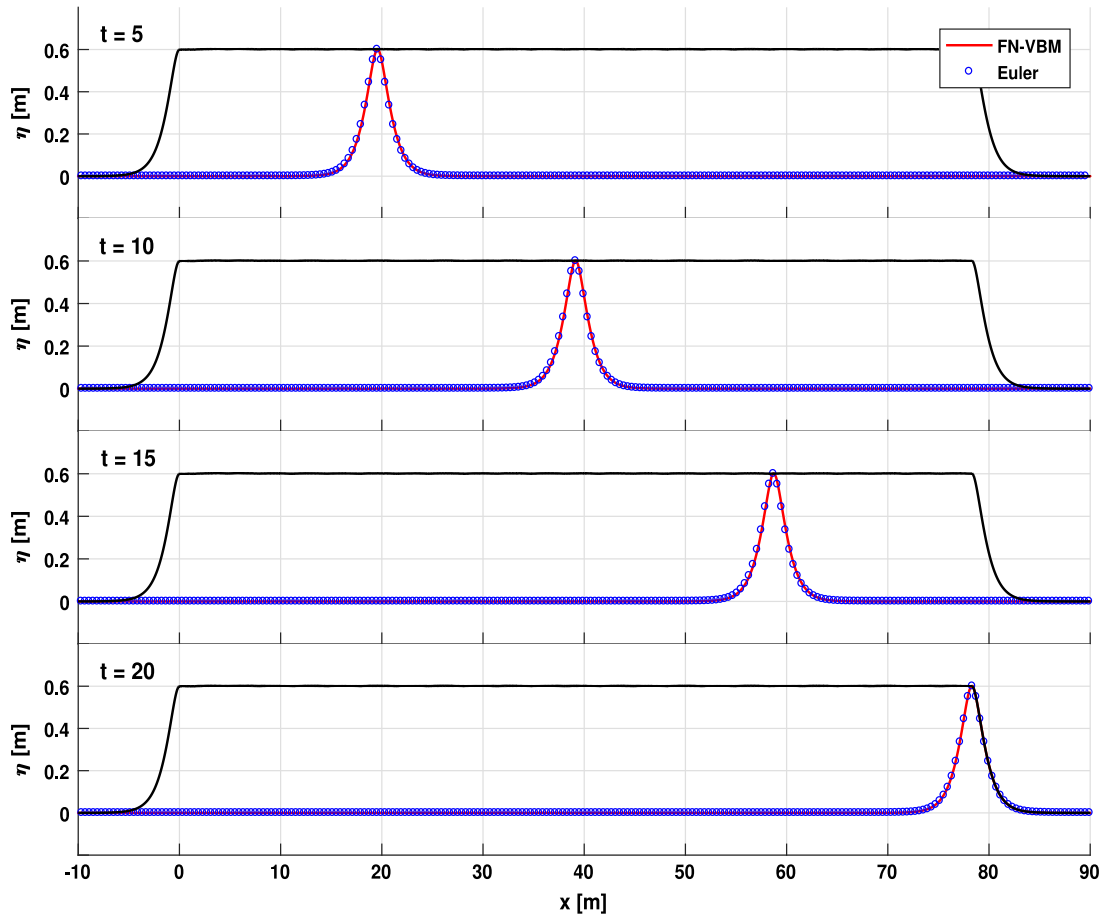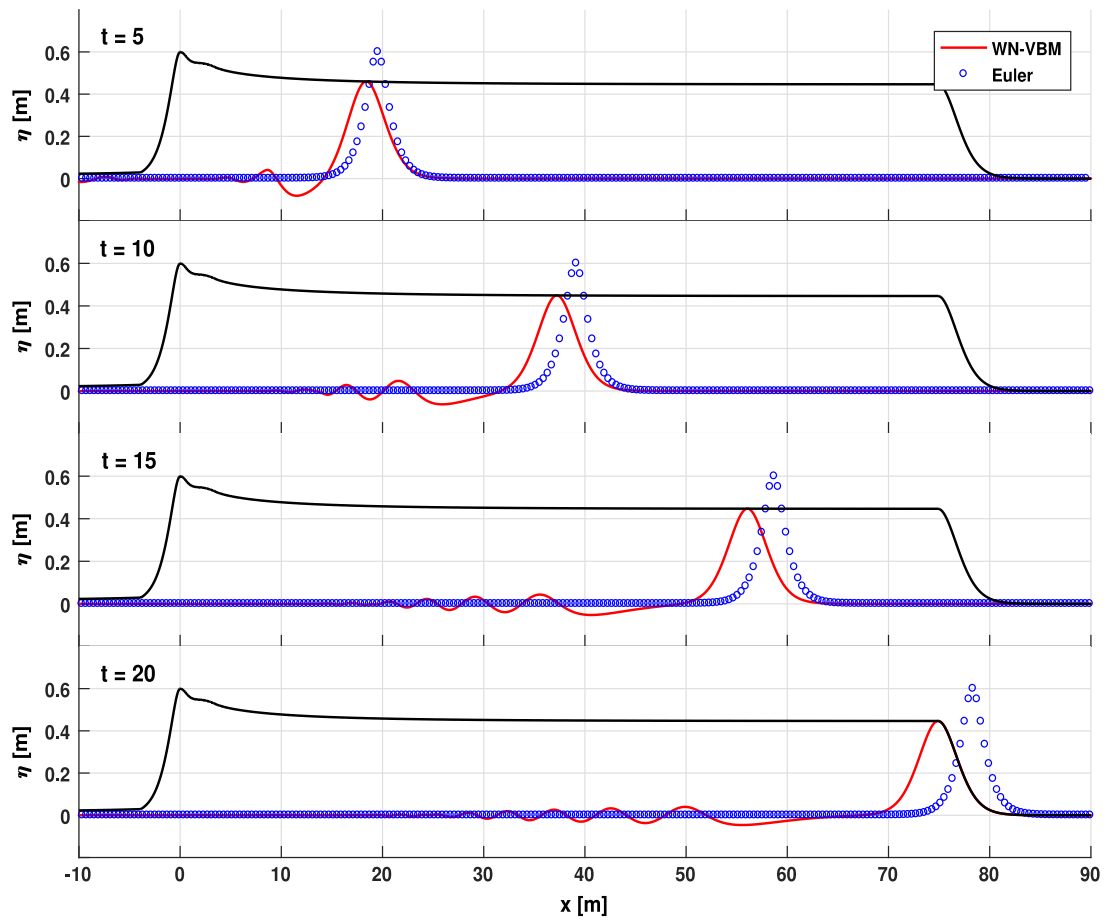
**Fig. 5.** Simulation results of the FN-VBM (red, solid) with solitary wave solution of Euler equations (circles) for $t = 5, 10, 15, 20$ and the Maximum Temporal Crest (black, dash). (For interpretation of the references to colour in this figure legend, the reader is referred to the web version of this article.)

**Table 1**
Comparison weakly (WN) and fully (FN) nonlinear VBM simulations.

| Position | Correlation | | Variance-quotient | |
|---|---|---|---|---|
| | WN–VBM | FN–VBM | WN–VBM | FN–VBM |
| W2 | 0.92 | 0.96 | 0.91 | 0.92 |
| W3 | 0.90 | 0.96 | 0.90 | 0.90 |
| W4 | 0.82 | 0.95 | 0.90 | 0.91 |
| W5 | 0.63 | 0.95 | 0.93 | 0.93 |

### 4.3. Harmonic wave propagation over submerged bar

Propagation over a submerged bar is known to test the nonlinearity and accurate dispersion of a wave model, as shown in experimental studies by Beji and Battjes [28], Luth et al. [32], Ohyama et al. [33], and Zou et al. [34]. When waves propagate over the front slope of a bar, higher harmonic bound waves are introduced and the waves become higher and steeper. Above the top of the bar, the bound harmonics become free harmonics while on the back slope, the wave energy is transferred back from higher harmonics to lower harmonics and more bound harmonics will be released. Therefore the nonlinearity of the model is important to generate higher harmonics and the accurate dispersion of the model is important to handle the speed of these higher harmonics.

We will show results of simulations for 3 different experiments, referring to [27] for regular and irregular wave simulations over the Beji–Battjes bar.

#### 4.3.1. Luth et al. experiment [32]

In the experiment of Luth et al. [32] the bar geometry is exactly the same as in the Beji and Battjes experiment [28] which has a 1:20 front slope followed by a 2 m flat crest and a 1:10 back slope. The still water depth in front and after the bar is 80 cm

**Fig. 6.** Simulation results of the WN-VBM (red, solid) with solitary wave solution of Euler equations (circles) for $t = 5, 10, 15, 20$ and the Maximum Temporal Crest (black, dash). (For interpretation of the references to colour in this figure legend, the reader is referred to the web version of this article.)
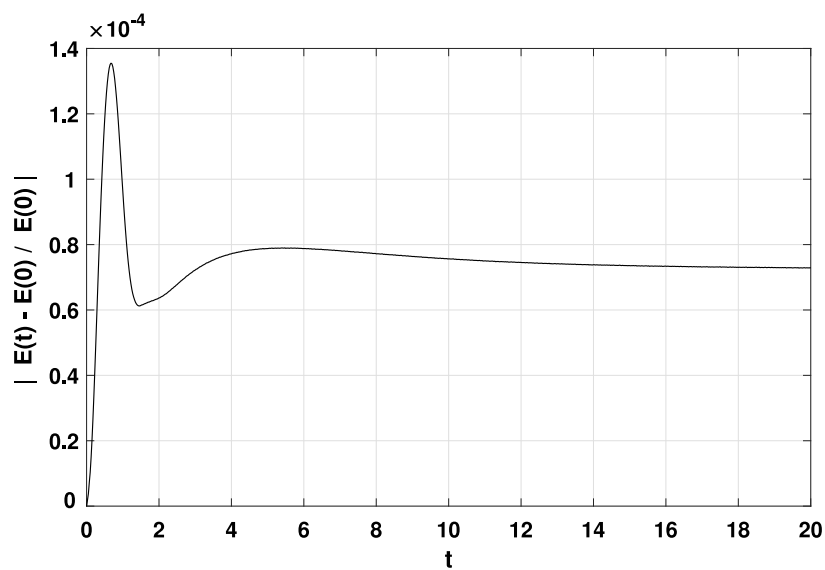


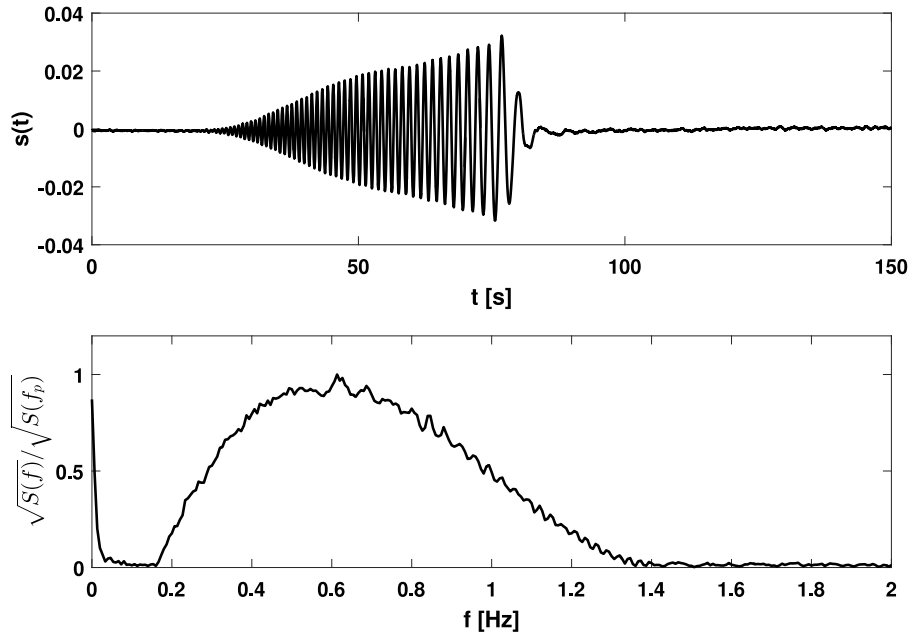**Fig. 7.** The total energy error relative to initial total energy for FN-VBM simulation.

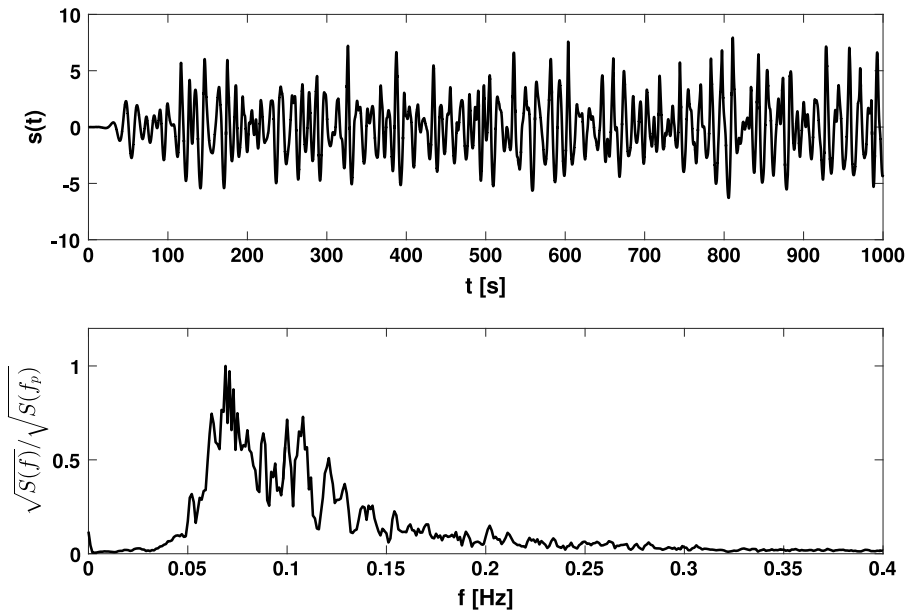**Fig. 8.** The initial signal (upper plot) and the amplitude spectrum (lower plot) of the Focusing Wave Group experiment.
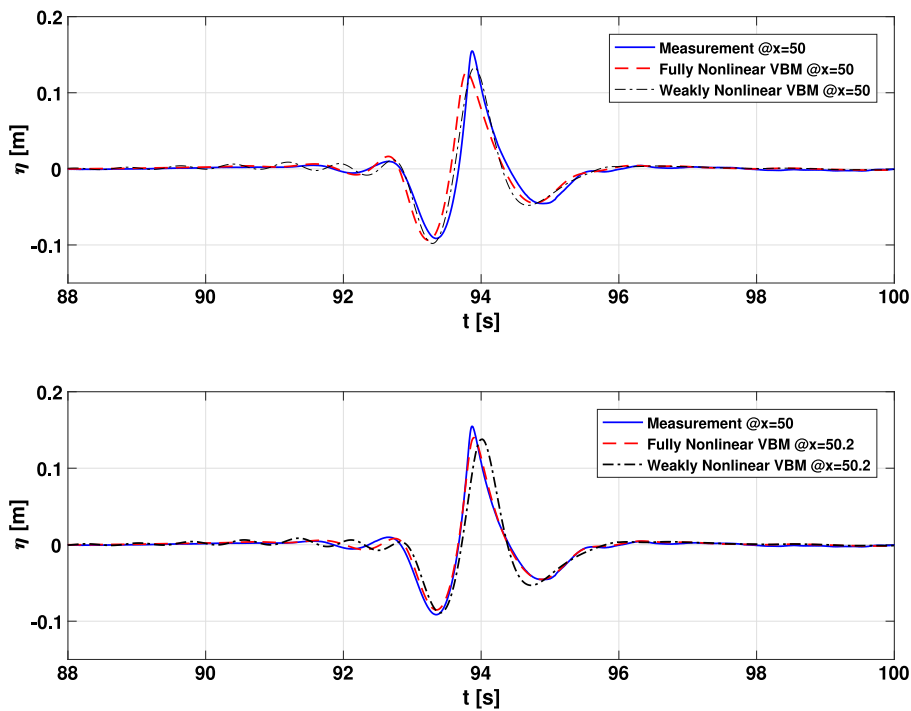


**Fig. 9.** Comparison of the FN-VBM (red, dash) at position $x = 50$ m (upper plot) and $x = 50.2$ m (lower plot) with measurement of the Focusing Wave Group experiment at position $x = 50$ m. (For interpretation of the references to colour in this figure legend, the reader is referred to the web version of this article.)

and it is 20 cm above the bar. In the present discussion we rescaled everything to the geometry used by Beji and Battjes [28], i.e. we use the linear scale factor of two so that the initial depth of 40 cm is used. The layout of the scaled experimental setup is shown in Fig. 14, with the waves propagating from left to right. There are eleven wave gauges where the wave elevation

**Comparison Weakly and Fully Nonlinear VBM, MTA & profile @ time: 94.2 [s]**
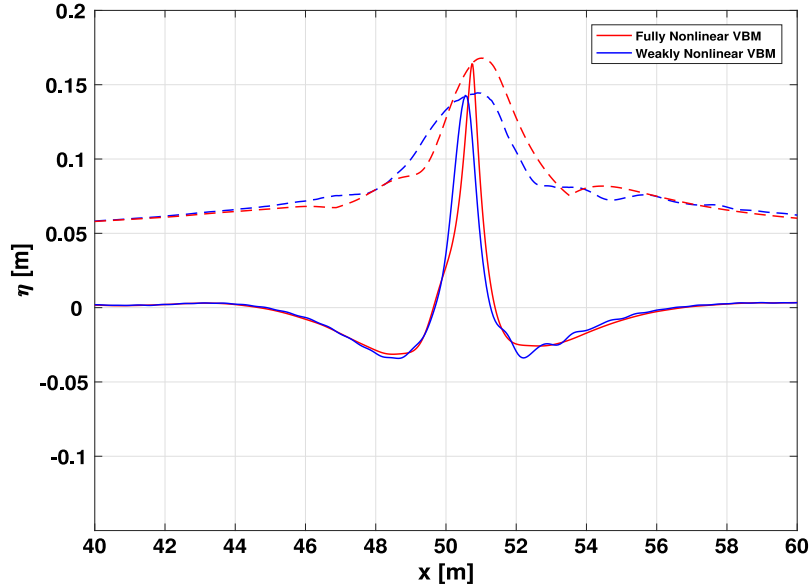


**Fig. 10.** Spatial wave profiles for WN-VBM (blue, solid), and for FN-VBM (red, solid) at time $t = 94.2$ s and the Maximum Temporal Amplitudes for WN-VBM (blue, dash) and FN-VBM (red, dash). (For interpretation of the references to colour in this figure legend, the reader is referred to the web version of this article.)



**Fig. 11.** The initial signal (upper plot) and the amplitude spectrum (lower plot) of the Deep Water Experiment.

is measured: W1 = 2.0, W2 = 4.0, W3 = 5.7, W4 = 10.5, W5 = 12.5, W6 = 13.5, W7 = 14.5, W8 = 15.7, W9 = 17.3, W10 = 19.0, W11 = 21.0, see Fig. 14. There are three cases, case A, B and C, with different incident wave condition. Since in case B wave breaking occurred, we focus on test cases A and C of the experiment: Case A has wave period $T = 2.02$ s and wave height $H = 2$ cm and case C has period $T = 1.01$ s, wave height $H = 4.1$ cm.

Fig. 15 shows the comparison between simulation and measurement. For case A, the simulation shows good agreement in both phase and amplitude. For case C, the simulated waves propagate somewhat too fast (around 0.1 s) in the downward sloping part; in other aspects, the simulations give good results.
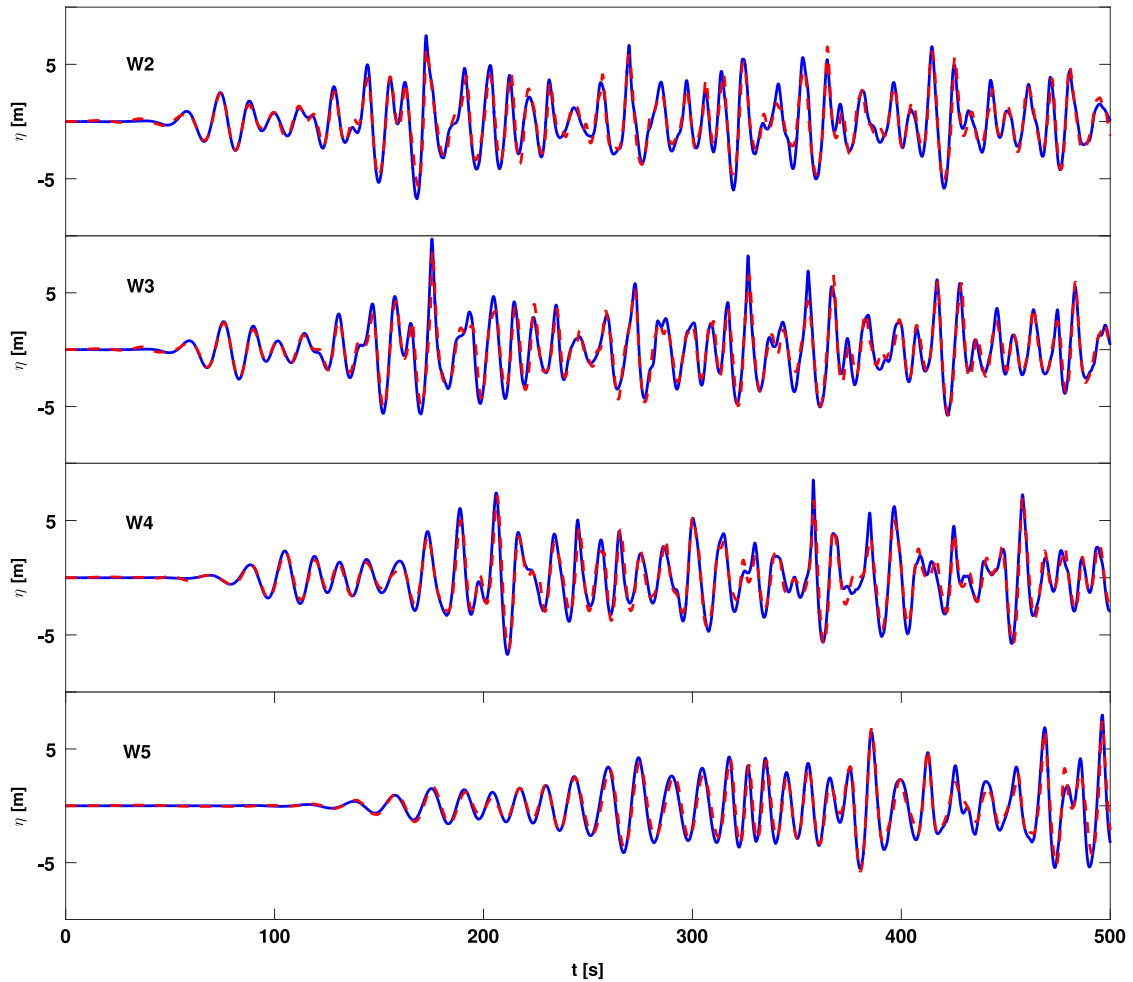
**Fig. 12.** Comparisons for Deep Water Experiment between FN-VBM (red, dash) and measurement (blue, solid) at positions W2, $x = 275.4$ m; W3, $x = 312.4$ m; W4, $x = 642.6$ m; W5, $x = 1593.4$ m for the interval (0;500) s. (For interpretation of the references to colour in this figure legend, the reader is referred to the web version of this article.)

### 4.3.2. Ohyama et al. experiment [33]

Experiments conducted by Ohyama et al. [33] in a wave flume of 65 m long and 1 m wide deal with a submerged bar that has a very steep 1:2 slope in front and at the back of the bar. The still water depth in the deeper region is 0.5 and 0.15 m on the top of bar. The distance from a piston-type wavemake to the centre of the bar is 28.3 m. At the end of the wave flume, there is a wave absorber. Measurements of the surface elevations were completed before reflected waves from the bar reached the wave generator. The location of the stations and other dimensions can be seen in Fig. 16.

Six different incident wave conditions were performed: three different wave periods 1.34, 2.01, 2.68 s, each with two different wave amplitudes 1.25, 2.5 cm. All these conditions lead to non-breaking waves. In this paper we focus on the three cases with the highest amplitudes 2.5 cm, denoted by case 2, 4 and 6 in Ohyama et al. [33]. Due to the steep slopes, the simulation introduces very high frequency noise which was filtered out. Fig. 17 show comparisons of FN-VBM simulations with the measurement data. Overall, the simulations give a good agreement with the measurement data.

### 4.3.3. Zou et al. experiment [34]

This experiment was conducted by Zou et al. [34] for two types of submerged bars. We refer to the first type as Case A which has a 1:10 front slope and 1:2 back slope, and Case B has 1:2 front slope and 1:10 back slope. The still water depth is 40 cm in front of the bar and 10 cm above the bar. The layout of the experiment and the position of the wave gauges is given in Fig. 18. Here, we only consider the experiment with short waves with period 1.3 s and wave height 2 cm, to restrict to the strongest dispersive and nonlinear effects.

Figs. 19 and 20 show comparison between simulations and measurements for case A and case B, respectively. In both cases, discrepancies in phase between measurement and simulation are observed above the down slope. However, the phase difference is still reasonable for practical use in ocean engineering.
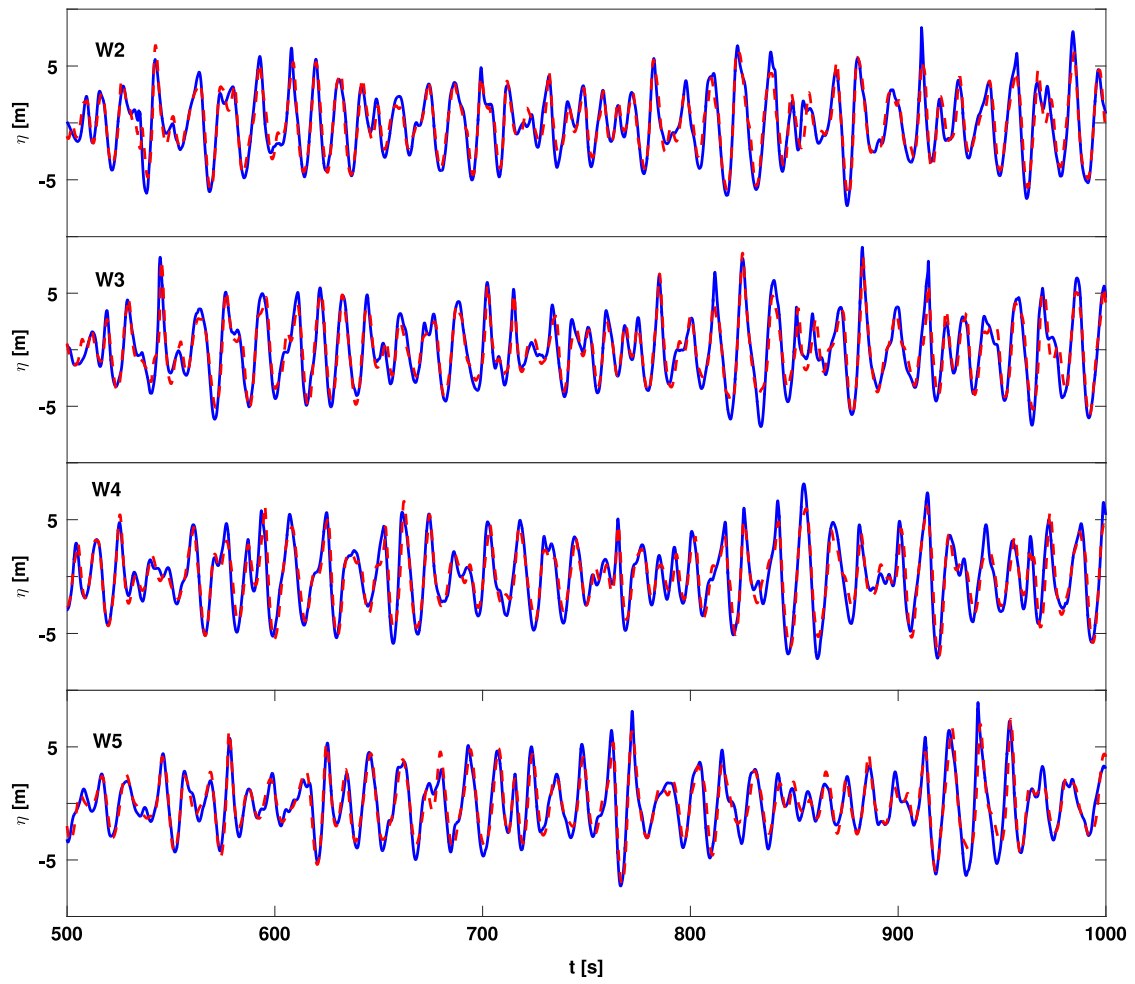
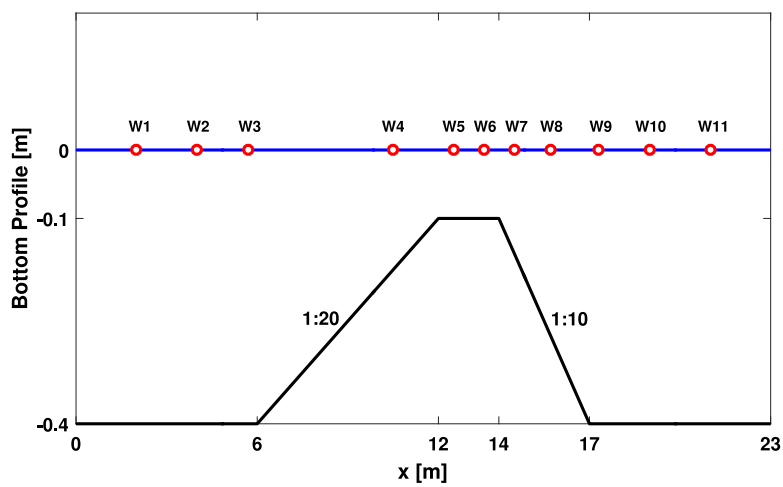**Fig. 13.** Same as Fig. 8 now for the interval (500; 1000) s.



**Fig. 14.** Lay out of Luth et al. experiment [32] with the location of wave gauges.
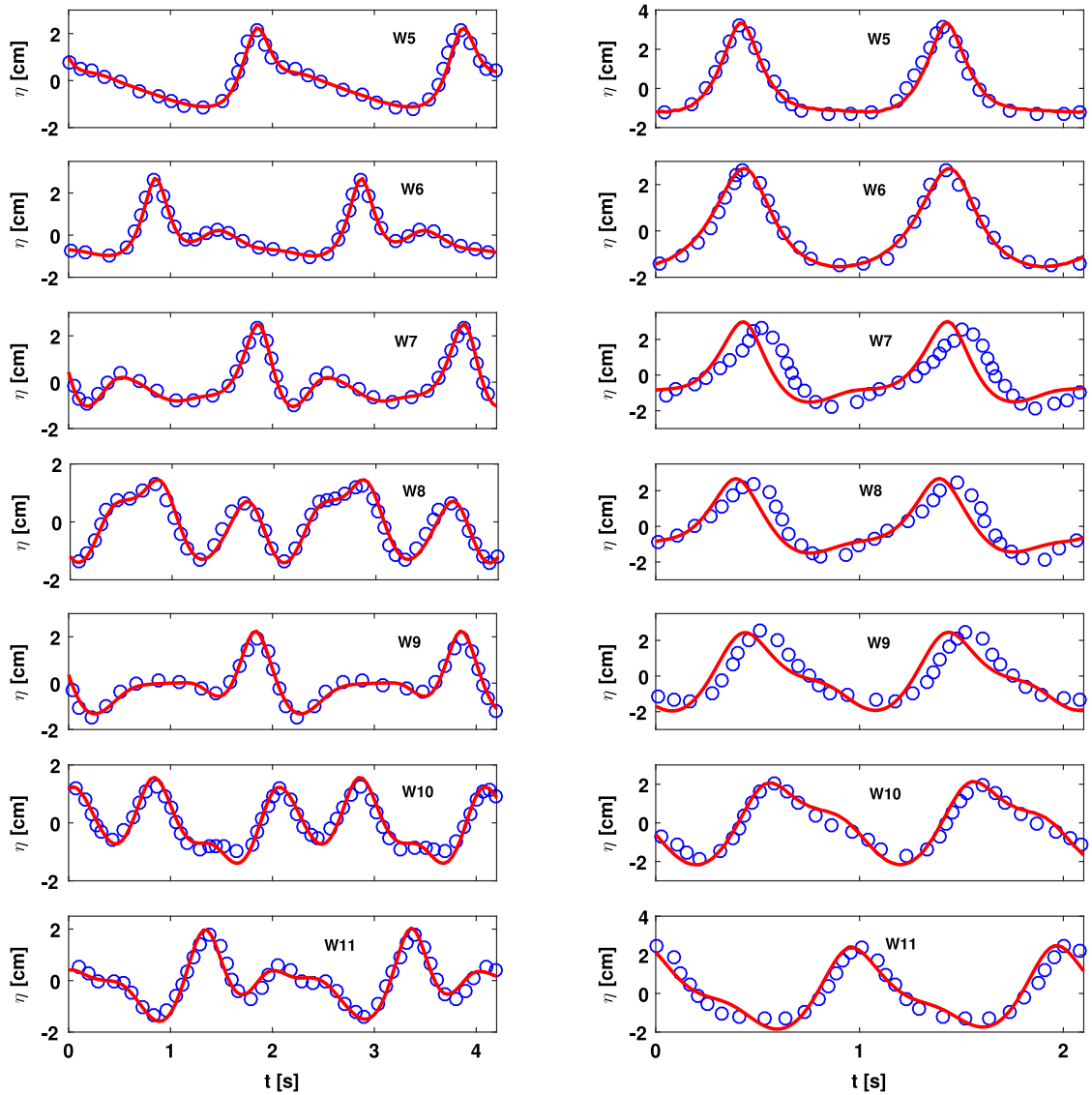
**Fig. 15.** Comparisons for Luth et al. experiment [32] between FN-VBM (red, solid) and measurement (circles). Left: case A; Right: case C. (For interpretation of the references to colour in this figure legend, the reader is referred to the web version of this article.)

### 4.4. Harmonic wave propagation over a shoal

The two cases considered here deal with shoaling of waves.

#### 4.4.1. Berkhoff et al. experiment [35]

Experiments conducted by Berkhoff et al. [35] has an elliptical shoal on a plane beach with a slope of 1 : 50. The waves are generated from the deeper part and at the other end the wave energy is absorbed. Physically, waves experience almost complete transformation caused by shoaling, refraction and diffraction for which dispersive and nonlinear effects are important. The experiment has been used for verifying various numerical wave models (Dingemans [36]).

The model setup and the measurement sections are shown in Fig. 21. An elliptic shoal is placed on the slope and the entire slope is turned over an angle 20° with the $y$-axis. Let $(x', y')$ be the slope-oriented coordinates which are related to the $(x, y)$ coordinate system by the rotation over $-20°$. The slope is described in units of metres by:

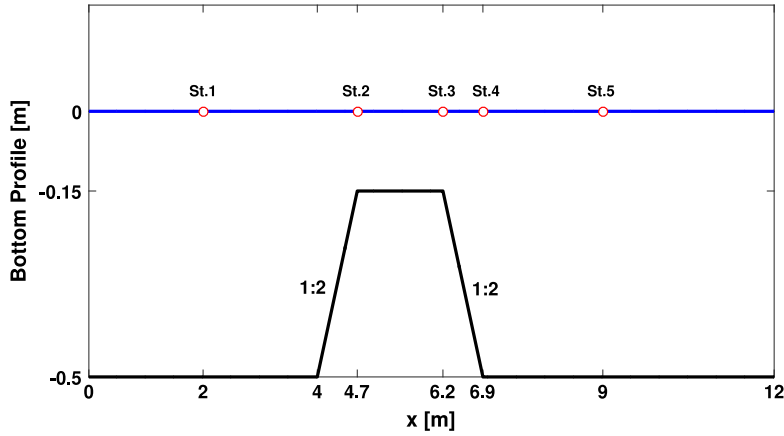$$h = \begin{cases} 0.45, & x' < -5.84 \\ max(0.10, 0.45 - 0.02(5.84 + x')), & x' \geq 5.84. \end{cases} \tag{22}$$

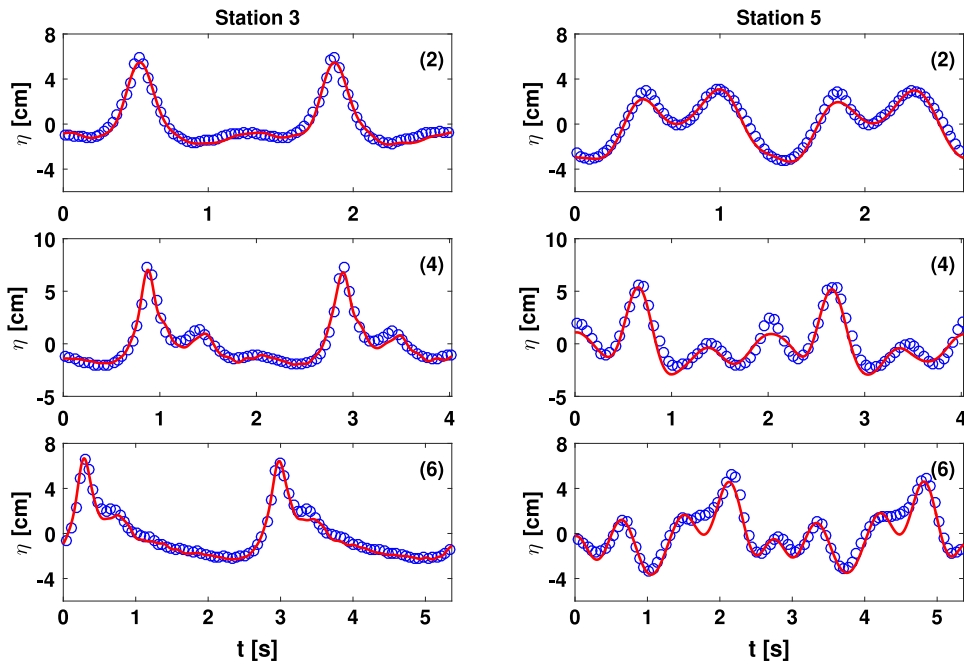**Fig. 16.** Lay out of Ohyama et al. experiment [33] with the location of wave gauges.



**Fig. 17.** Comparisons for Ohyama et al. experiment [33] between FN-VBM (red, solid) and measurement (circles) at stations 3 (left) and 5 (right). Upper row case 2, middle row case 4 and lower row case 6. (For interpretation of the references to colour in this figure legend, the reader is referred to the web version of this article.)

To avoid breaking waves, we use a minimum depth of 0.1 m instead of shoreline boundary. The boundary of the shoal is given by

$$\left(\frac{x'}{3}\right)^2 + \left(\frac{y'}{4}\right)^2 = 1 \tag{23}$$

and the shoal thickness is given by

$$d = -0.3 + 0.5\sqrt{1 + \left(\frac{x'}{3.75}\right)^2 + \left(\frac{y'}{5}\right)^2}. \tag{24}$$

Incident monochromatic waves with period 1.0 s and amplitude 2.32 cm propagate in the *x*-direction. The lateral boundary conditions (at $y = 0$ and $y = 20$) are set to be a fully reflective wall, while at the right end waves are absorbed by
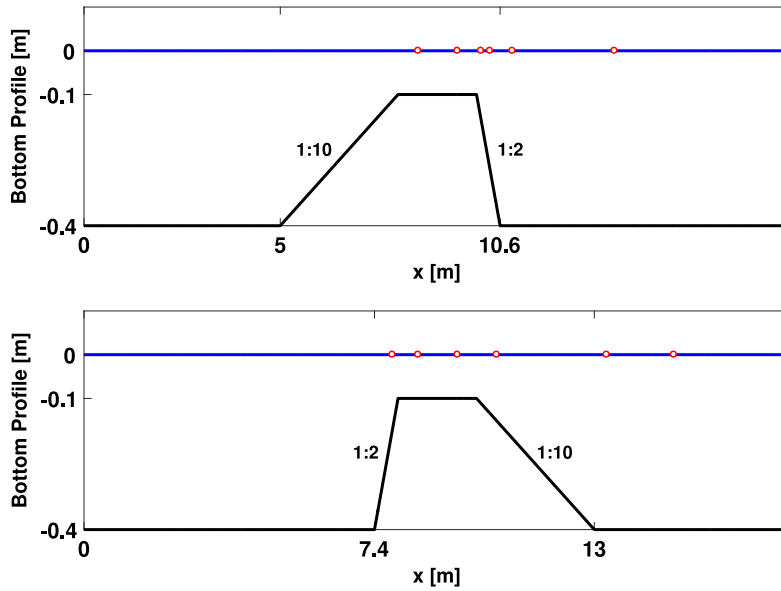
**Fig. 18.** Lay out of Zou et al. experiment [34] with the location of wave gauges. Upper plot : Case A; Lower plot : Case B.
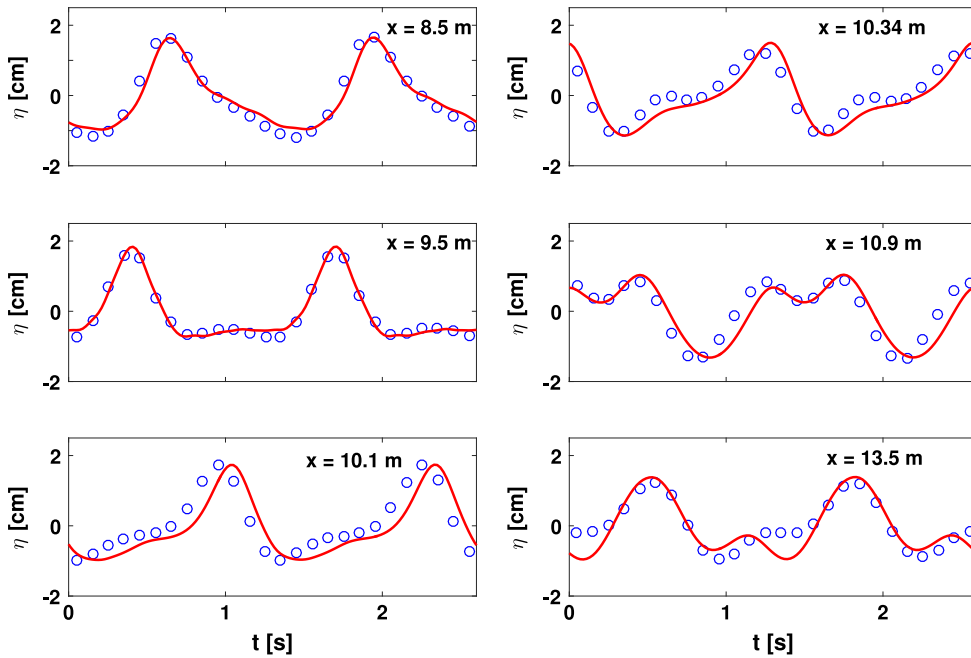


**Fig. 19.** Comparisons for Zou et al. experiment [34] case A between FN-VBM (red, solid) and measurement (circles). (For interpretation of the references to colour in this figure legend, the reader is referred to the web version of this article.)

a sponge layer of 4 m wide. We use an unstructured triangular grid with maximum grid space is 0.1 m. In this simulation, we still consider only two profiles in FN-VBM.

Compared to Adytia [37], here the weakly nonlinear version of VBM is replaced by FN-VBM for simulations over a time interval of 40 wave periods. The wave height of the simulation is obtained as the average from the last five waves from $t = 35$ s to $t = 40$ s.

Fig. 22 shows the simulation results compared to measurements at eight sections using WN-VBM and FN-VBM. For FN-VBM, the peak wave heights are well predicted, even at the most difficult Sections 3, 4 and 5. A small discrepancy is found near $y = 8$ in Section 5 where the waves are slightly shifted to the negative $y$-direction. This may be caused by contributions
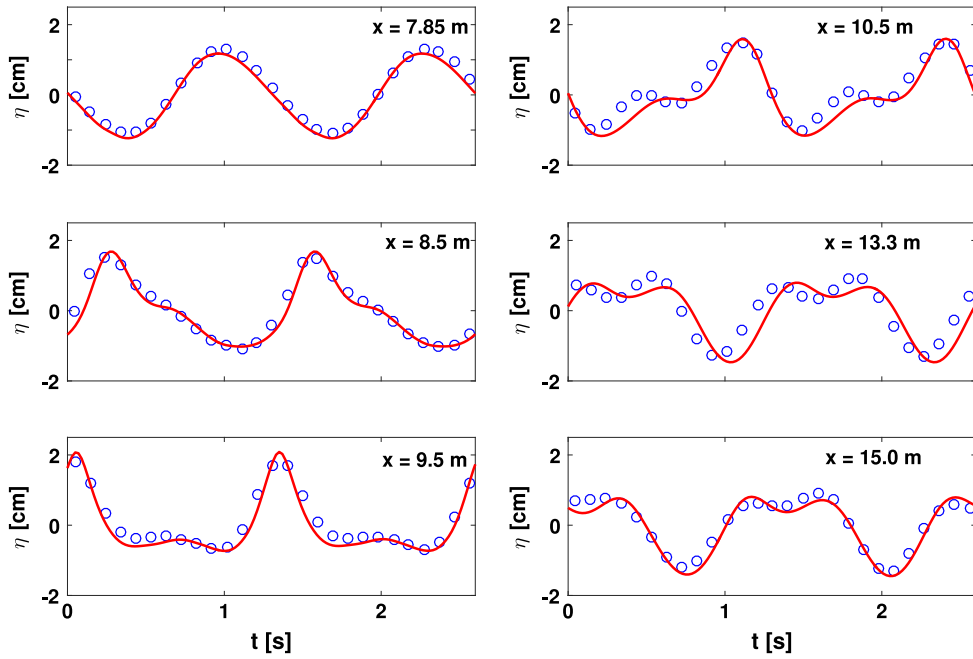
**Fig. 20.** Comparisons for Zou et al. Experiment [34] case B between FN-VBM (red, solid) and measurement (circles). (For interpretation of the references to colour in this figure legend, the reader is referred to the web version of this article.)
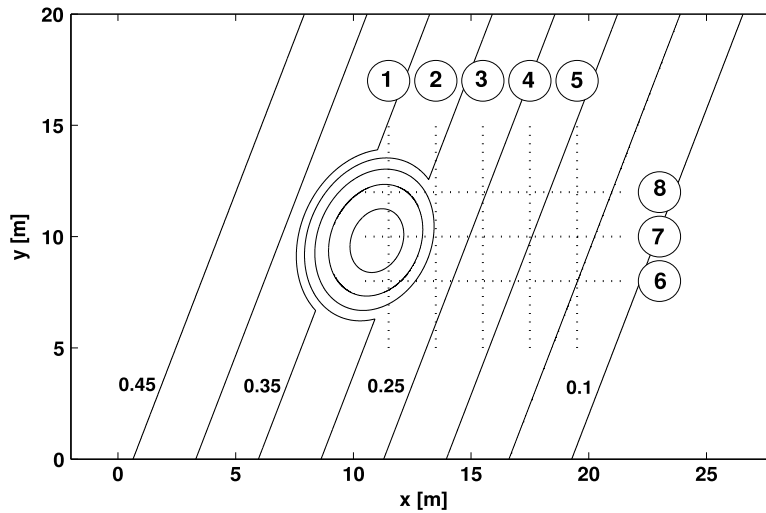


**Fig. 21.** Bottom topography for experiment of Berkhoff et al. [35]. Dotted lines (labelled from 1 to 8) indicate sections in Fig. 18.

of 3rd and 4th order higher harmonics which are not well defined by the dispersion with two profiles. Overall, the comparison between the FN-VBM and measurements show a good agreement, essentially better at all cross sections than the simulations with WN-VBM.

### 4.4.2. Chawla et al. experiment [38]

Chawla et al. [38] performed experiments in a wave basin of approximately 18 m long and 18.2 m wide with a circular shoal placed on the flat bottom. Incident waves are generated by three dimensional wavemakers at one end consisting of 34 flap type paddles, and at the other end waves are absorbed. The experimental data is given by one longitudinal transect going through the shoal (A-A) and six transverse transects (B-B, C-C, D-D, E-E, F-F and G-G); the layout of the experiment and the transects are shown in Fig. 23.
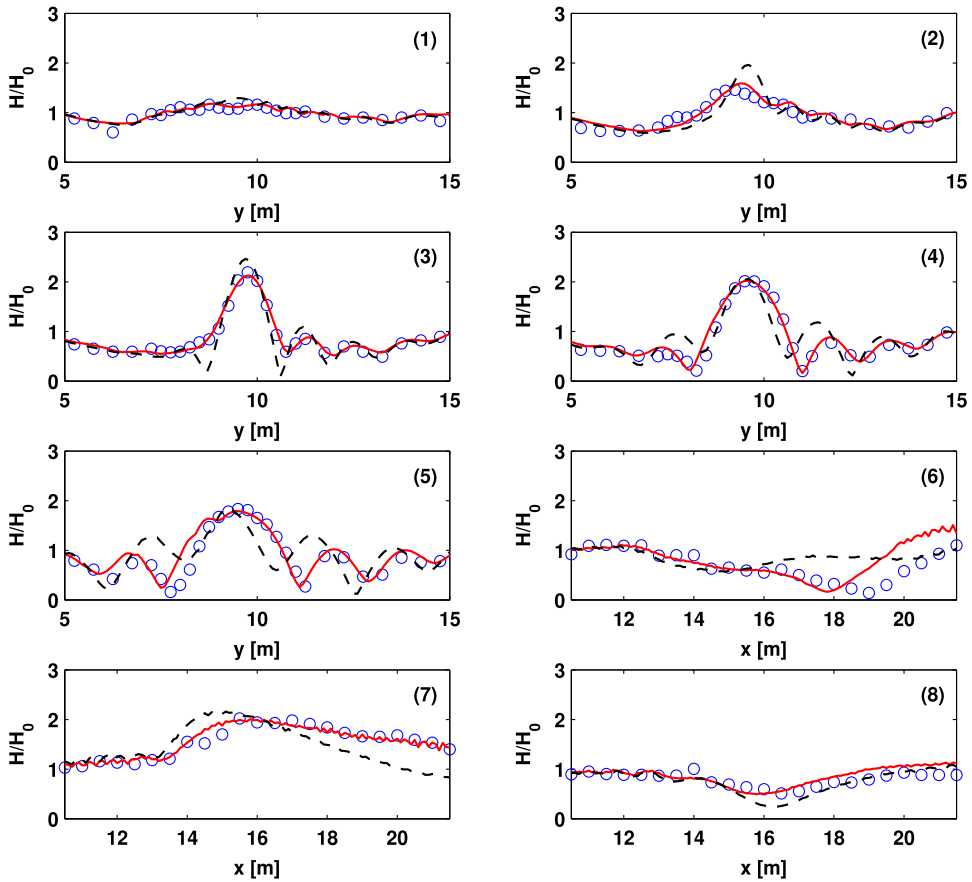
**Fig. 22.** Comparisons of the normalized wave height for Berkhoff et al. [35] experiment between WN-VBM (black, dash), FN-VBM (red, solid) and measured (circles) at eight sections. (For interpretation of the references to colour in this figure legend, the reader is referred to the web version of this article.)

The circular shoal has a radius of 2.57 m and the centre is located at $x = 5$ m and $y = 8.98$ m. The water depth above the submerged shoal is given by

$$h = h_0 + 8.73 - \sqrt{9.1^2 - (x - 5)^2 - (y - 8.98)^2} \tag{25}$$

with $h_0 = 0.45$ m the constant water depth of the wave basin and $h = 0.08$ m above the top of the shoal.

From four non-breaking harmonic wave experiments we only focus on TEST 4 which has wave height 1.18 cm, and wave period 1 s. The lateral boundaries at $y = 0$ m and $y = 18.2$ m are set to be a fully reflective wall, and we use 4 m wide sponge layer to represent the absorbing beach. An unstructured triangular grid with maximum grid space 0.1 m is used; the same parameters $\kappa$ are used as in Berkhoff's experiment since the wave period and water depth at the wavemaker are the same.

The FN-VBM simulation is run for 40 s, during which the wave field reaches a stable condition; as before, the computed wave height is obtained by taking the average from the five last waves from $t = 35$ s to $t = 40$ s. Comparisons of normalized wave amplitudes with respect to incoming wave between the model and experiment data through all transects are shown in Fig. 24.

Although the incident wave condition and the water depth at the wavemaker is similar with Berkhoff et al. experiment, this experiment leads to stronger focusing waves. In transect A-A and E-E, the amplification factor of the wave height reaches up to 2.7, considerably larger compared to Berkhoff's experiment for which the amplification factor is around 2.

## 5. Conclusion

A fully nonlinear Variational Boussinesq model (FN-VBM) with multiple vertical profiles has been derived. In the derivation, bottom variations are dealt with in a quasi-homogeneous way. With this approximation, FN-VBM still gives acceptable results even for very steep slopes (up to 1:2).

Due to the flexibility to choose the number of vertical profiles and the parameters $\kappa$, the dispersion quality can be adjusted depending on the case. In this paper, we improved the optimization criterion for the parameters $\kappa$ compared to Lakthurov
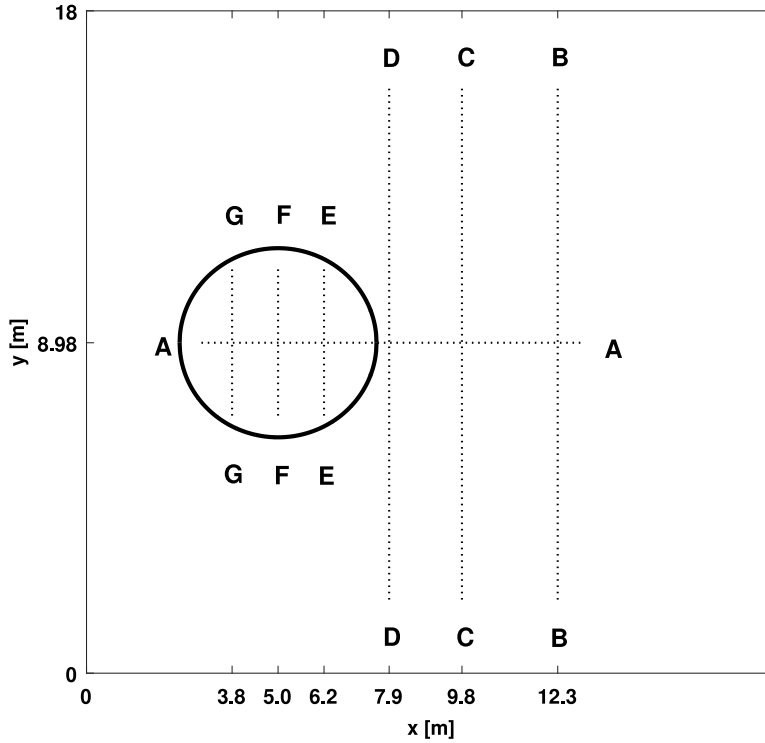
**Fig. 23.** Layout of the experimental setup. Dotted lines (labelled from A to G) indicate sections in Fig. 20.

et al. [20]. For linear evolution above flat bottom, the spectrum is independent of time. However, the initial spectrum can be deformed when strong nonlinear effects and/or bottom variations are present. If the spectrum is deformed, it may be more accurate to find optimized parameters based on the deformed spectrum (a trial simulation will provide an approximation of the deformed spectrum).

The results of the test cases show that FN-VBM has good dispersive properties and can simulate very steep waves, in several cases considerably better that the weakly-nonlinear VBM.

### Acknowledgements

### Appendix

Here we present the explicit expressions for the coefficients in the kinetic energy when using the hyperbolic-cosine functions as vertical profiles in (9). We use the notation

$$H = \eta + h, \text{ and } T_m = \tanh(\kappa_m H)$$

in the following expressions for the integrals in (12) and their derivatives with respect to $\eta$.

For the case of multiple profiles for $i \neq j$

$$\alpha_{ij} = \frac{\kappa_j T_j - \kappa_i T_i}{\kappa_j^2 - \kappa_i^2} - \frac{T_i}{\kappa_i} - \frac{T_j}{\kappa_j} + H$$

$$\partial_\eta \alpha_{ij} = \frac{\kappa_j^2 T_i^2 - \kappa_i^2 T_j^2}{\kappa_j^2 - \kappa_i^2}$$

$$\gamma_{ij} = \frac{\kappa_i \kappa_j \left[ \kappa_j T_i - \kappa_i T_j \right]}{\kappa_j^2 - \kappa_i^2}$$
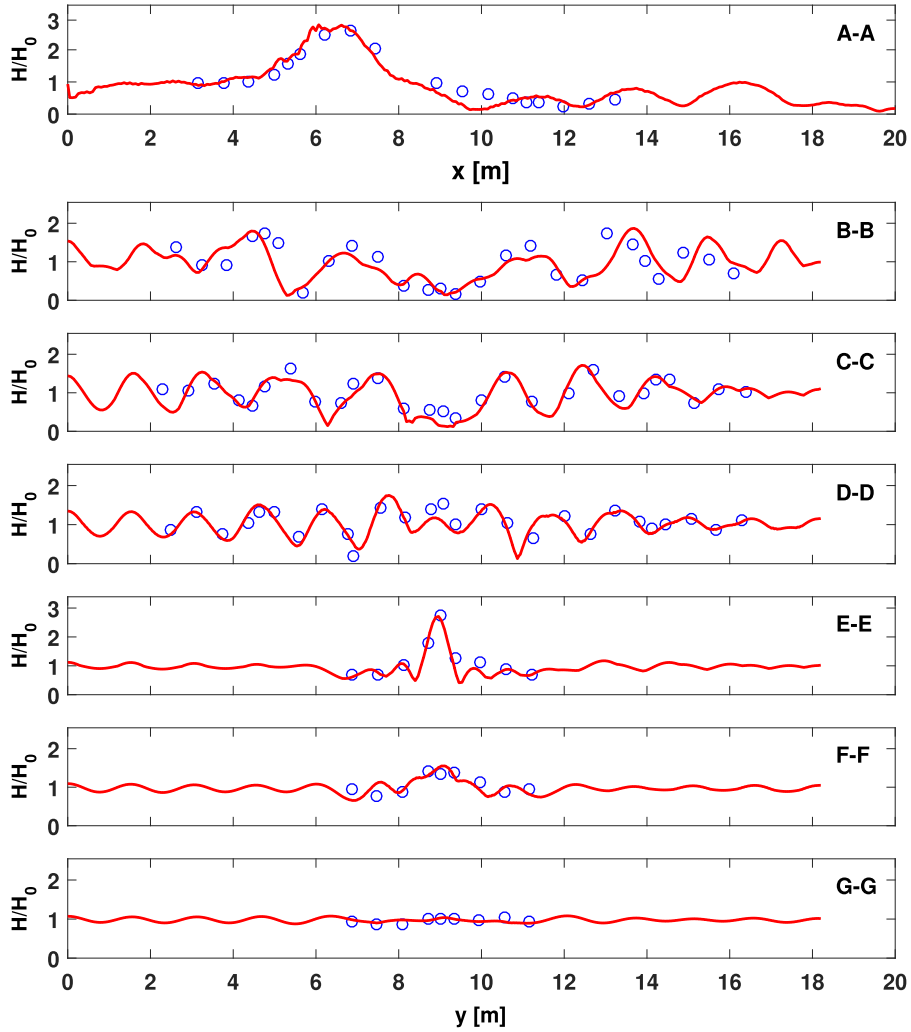
**Fig. 24.** Comparisons of normalized wave heights between FN-VBM (red, solid) and measured (circles) at seven sections. (For interpretation of the references to colour in this figure legend, the reader is referred to the web version of this article.)

$$\partial_\eta \gamma_{ij} = \frac{\kappa_i^2 \kappa_j^2 \left[ T_j^2 - T_i^2 \right]}{\kappa_j^2 - \kappa_i^2}$$

$$\varepsilon_{ij} = \frac{\kappa_i \left[ \kappa_j T_j T_i - \kappa_i T_j^2 \right]}{\kappa_j^2 - \kappa_i^2}$$

$$\partial_\eta \varepsilon_{ij} = \frac{\kappa_i \kappa_j \left[ \kappa_j T_i \mathrm{sech}^2(\kappa_j H) - \kappa_i T_j \left( 2\, \mathrm{sech}^2(\kappa_j H) - \mathrm{sech}^2(\kappa_i H) \right) \right]}{\kappa_j^2 - \kappa_i^2}$$

$$\theta_{ij} = \frac{\kappa_i \kappa_j T_i T_j \left[ \kappa_j T_j - \kappa_i T_i \right]}{\kappa_j^2 - \kappa_i^2}$$

$$\partial_\eta \theta_{ij} = \frac{2 \kappa_i \kappa_j T_i T_j \left[ \kappa_j^2 \mathrm{sech}^2(\kappa_j H) - \kappa_i^2 \mathrm{sech}^2(\kappa_i H) \right]}{\kappa_j^2 - \kappa_i^2} + \frac{\kappa_i^2 \kappa_j^2 \left[ T_j^2 - T_i^2 \right]}{\kappa_j^2 - \kappa_i^2}.$$

For $i = j$ the results are obtained by taking the limit in the above expressions

$$\alpha_{ii} = -\frac{1.5\, T_i}{\kappa_i} + H \left[ 1 + 0.5\, \mathrm{sech}^2(\kappa_i H) \right]$$

$$\partial_\eta \alpha_{ii} = T_i^2 - \kappa_i H\, T_i \mathrm{sech}^2(\kappa_i H)$$

$$\beta_i = \frac{T_i}{\kappa_i} - H$$

$$\partial_\eta \beta_i = -T_i^2$$

$$\gamma_{ii} = 0.5\,\kappa_i \left[ T_i - \kappa_i H \mathrm{sech}^2(\kappa_i H) \right]$$

$$\partial_\eta \gamma_{ii} = \kappa_i^3 H T_i \mathrm{sech}^2(\kappa_i H)$$

$$\xi_i = -T_i^2$$

$$\partial_\eta \xi_i = -2\,\kappa_i T_i \mathrm{sech}^2(\kappa_i H)$$

$$\varepsilon_{ii} = 0.5\,T_i \left[ T_i - \kappa_i H \mathrm{sech}^2(\kappa_i H) \right]$$

$$\partial_\eta \varepsilon_{ii} = 0.5\,\kappa_i \mathrm{sech}^2(\kappa_i H) \left[ T_i + \kappa_i H \left( 3\,T_i^2 - 1 \right) \right]$$

$$\theta_{ii} = 0.5 \kappa_i T_i^2 \left[ T_i + \kappa_i H \mathrm{sech}^2(\kappa_i H) \right]$$

$$\partial_\eta \theta_{ii} = \frac{\kappa_i^2 T_i \left[ 2\,T_i + \kappa_i H \left( \mathrm{sech}^2(\kappa_i H) - T_i^2 \right) \right]}{\cosh^2(\kappa_i H)}.$$

# References

[1] J. Boussinesq, Theorie des ondes et des remous qui se propagent le long d'un canal rectangulaire horizontal, en communiquant au liquide contenu dans ce canal des vitesses sensiblement pareilles de la surface au fond, J. Math. Pures Appl. 17 (1872) 55–108.

[2] D.H. Peregrine, Long waves on a beach, J. Fluid Mech. 27 (1967) 815–820.

[3] P.A. Madsen, R. Murray, O.R. Sorensen, A new form of Boussinesq equations with improved linear dispersion characteristics, Coastal Eng. 15 (1991) 371–388.

[4] O. Nwogu, An alternative form of the Boussinesq equations for nearshore wave propagation, J. Waterw. Port Coast. Ocean Eng. 119 (1993) 618–638.

[5] V.E. Zakharov, Stability of periodic waves of finite amplitude on the surface of a deep fluid, J. Appl. Mech. Tech. Phys. 9 (1968) 190–194.

[6] L.J.F. Broer, On the Hamiltonian theory of surface waves, Appl. Sci. Res. 29 (1974) 430–446.

[7] J.W. Miles, On Hamiltonian principle for surface waves, J. Fluid Mech. 83 (1977) 153–158.

[8] H. Bateman, Notes on a differential equation which occurs in the two-dimensional motion of a compressible fluid and the associated variational problems, Proc. R. Soc. Lond. Ser. A Math. Phys. Eng. Sci. 125 (1929) 598–618.

[9] J.C. Luke, A variational principle for a fluid with a free surface, J. Fluid Mech. 27 (1967) 395–397.

[10] D.G. Dommermuth, D.K.P. Yue, A high-order spectral method for the study of nonlinear gravity waves, J. Fluid Mech. 184 (1987) 267–288.

[11] B.J. West, K.A. Brueckner, R.S. Janda, D.M. Milder, R.L. Milton, A new numerical method for surface hydrodynamics, J. Geophys. Res. 92 (C11) (1987) 11803–11824.

[12] W. Craig, C. Sulem, Numerical simulation of gravity waves, J. Comput. Phys. 108 (1993) 73–83.

[13] W.J.D. Bateman, C. Swan, P.H. Taylor, On the efficient numerical simulation of directionally spread surface water waves, J. Comput. Phys. 174 (2001) 277–305.

[14] P. Guyenne, D.P. Nicholls, A high-order spectral method for nonlinear water waves over moving bottom topography, SIAM J. Sci. Comput. 30 (1) (2007) 81–101.

[15] L. Xu, P. Guyenne, Numerical simulation of three-dimensional nonlinear water waves, J. Comput. Phys. 228 (22) (2009) 8446–8466.

[16] J. Wilkening, V. Vasan, Comparison of five methods of computing the Dirichlet-Neumann operator for the water wave problem, in: Nonlinear Wave Equations: Analytic and Computational Techniques, in: Contemp. Math., vol. 635, Amer. Math. Soc., Providence, RI, 2015, pp. 175–210.

[17] H.A. Schaffer, Comparison of Dirichlet-Neumann operator expansions for nonlinear surface gravity waves, Coastal Eng. 55 (2008) 288–294.

[18] G. Klopman, E. van Groesen, M.W. Dingemans, A variational approach to Boussinesq modeling of fully non-linear water waves, J. Fluid Mech. 657 (2010) 36–63.

[19] D. Adytia, E. van Groesen, Optimized Variational 1D Boussinesq modelling of coastal waves propagating over a slope, Coastal Eng. 64 (2012) 139–150.

[20] I. Lakhturov, D. Adytia, E. van Groesen, Optimized variational 1D Boussinesq modelling for broad-band waves over flat bottom, Wave Motion 49 (2012) 309–322.

[21] L.J.F. Broer, Approximate equations for long wave equations, Appl. Sci. Res. 31 (1975) 377–395.

[22] L.J.F. Broer, E. van Groesen, J.M.W. Timmers, Stable model equations for long water waves, Appl. Sci. Res. 32 (1976) 619–636.

[23] G. Klopman, Variational Boussinesq Modeling of Surface Gravity Waves over Bathymetry (Ph.D. thesis), University of Twente, Enschede, The Netherlands, 2010.

[24] P.-O. Persson, G. Strang, A simple mesh generator in matlab, SIAM Rev. 46 (2) (2008) 329–345.

[25] H.A. van der Vorst, BI-CGSTAB: A fast and smoothly converging variant of BI-CG for the solution of nonsymmetric linear systems, SIAM J. Sci. Stat. Comput. 13 (2) (1992) 631–644.

[26] S.L. Lie, E. van Groesen, Embedded wave generation for the dispersive surface wave models, Ocean Eng. 80 (2014) 73–83.

[27] D. Adytia, . Lawrence, Fully nonlinear dispersive HAWASSI-VBM for coastal zone simulations, in: ASME 35th Int. Conference on Ocean, Offshore and Arctic Eng. OMAE. Busan, Korea, 2016.

[28] S. Beji, J.A. Battjes, Experimental investigation of wave propagation over a bar, Coastal Eng. 19 (1993) 151–162.

[29] G. Wei, J. Kirby, S. Grilli, R. Subramannya, A fully nonlinear Boussinesq model for surface waves. Part 1. Highly nonlinear unsteady waves, J. Fluid Mech. 294 (1995) 71–92.

[30] D. Dutykh, C. Clamond, Efficient computation of steady solitary gravity waves, Wave Motion 51 (2014) 86–99.

[31] I. Lakhturov, Optimization of Variational Boussinesq Models (Ph.D. thesis), University of Twente, Enschede, The Netherlands, 2013.

[32] H.R. Luth, G. Klopman, N. Kitou, Project 13 G: Kinematics of Waves Breaking Partially on an Offshore Bar; LDV Measurements for Waves with and Without a Net Onshore Current, Technical Report H1573. Delft Hydraulics, The Netherlands, 1994.

[33] T. Ohyama, W. Kiota, A. Tada, Applicability of numerical models to nonlinear dispersive waves, Coastal Eng. 24 (1995) 297–313.

[34] Z.L. Zou, K.Z. Fang, Z.B. Liu, Inter-Comparisons of Different Forms of Higher-Order Boussinesq Equations, in: Advanced Series on Ocean Eng., vol. 11, World Scientific, Singapore, 2010 (Chapter 8).

[35] J.C.W. Berkhoff, N. Booij, A.C. Radder, Verification of numerical wave propagation models for simple harmonic linear water waves, Coastal Eng. 6 (1982) 255–279.

[36] M.W. Dingemans, Water Wave Propagation over Uneven Bottoms, in: Advanced Series on Ocean Eng., vol. 13, World Scientific, Singapore, 1997.
[37] D. Adytia, Coastal Zone Simulations with Variational Boussinesq Modeling (Ph.D. thesis), University of Twente, Enschede, The Netherlands, 2012.
[38] A. Chawla, J.T. Kirby, Wave Transformation Over a Submerged Shoal, CACR Rep. No. 96-03, Department of Civil Engineering, University of Delaware, Newark, Delaware, 1996.